How extreme apparitions of the volcanic and anthropogenic south east Asian aerosol plume simultaneously trigger and sustain: El Niño and Indian Ocean Dipole events and drought in south eastern Australia . First attribution and mechanism

K. A. Potts[1]

[1]Kyna Keju Pty Ltd, Adelaide, South Australia.

Corresponding author: Keith Potts (Keith.Potts@bigpond.com)

Key Points:

- Volcanic aerosols over South East Asia have always triggered and sustained El Nino and IOD events and drought in south eastern Australia
- These volcanic aerosol plumes have been augmented by anthropogenic aerosols in recent decades especially from September to November
- The Last Millennium Ensemble and 23 models from CMIP6 incorporate aerosol levels over south east Asia which are far too low

Abstract

Volcanic aerosol plumes over south east Asia (SEAsia), and only over SEAsia, have always been the trigger and sustaining cause of: El Niño Southern Oscillation (ENSO) events which are the dominant mode of variability in the global climate; Australian and Indonesian droughts; increased global temperatures; and Indian Ocean Dipole (IOD) events. In recent decades this natural plume has been augmented by an anthropogenic plume which has intensified these events especially from September to November. Understanding the mechanism which enables aerosols over SEAsia, and only over SEAsia, to create ENSO events is crucial to understanding the global climate. I show that the SEAsian aerosol plume causes ENSO events by: reflecting/absorbing solar radiation which warms the upper troposphere; and reducing surface radiation which cools the surface under the plume. This inversion reduces convection in SEAsia thereby suppressing the Walker Circulation and the Trade Winds which causes the Sea Surface Temperature (SST) to rise in the central Pacific Ocean and creates convection there. This further weakens/reverses the Walker Circulation driving the climate into an ENSO state which is maintained until the SEAsian aerosols dissipate and the climate system relaxes into a non-ENSO state. Data from the Global Volcanism Program (151 years), the Last Millennium Ensemble (1,156 years), MERRA-2 (41 years) and NASA MODIS on Terra (21 years) demonstrates this connection with the Nino 3.4 and 1+2 SST, the Southern Oscillation Index, and three events commonly associated with ENSO: drought in south eastern Australia; the IOD and a warmer World.

Plain Language Summary

El Niño events, the greatest inter-annual variation in the global climate, are and always have been caused by volcanic aerosols in south east Asia. In recent decades the volcanic aerosols have been augmented by anthropogenic aerosols especially from September to November which has intensified ENSO events in these months. The same aerosol plume also creates drought in south eastern Australia and Indian Ocean Dipole events simultaneously. Volcanic, modelling, reanalysis and measured data all confirm these results.

1 Introduction

South East Asia (SEAsia) is a unique region with several attributes which enable SEAsia, and only SEAsia, to create and sustain El Niño Southern Oscillation Index (SOI) (ENSO) events and their associated effects such as drought in South Eastern Australia (SEAus) and Indian Ocean Dipole (IOD) events. SEAsia is a region which covers about 3% of the global surface and: hosted 26% of the eruptions in the Global Volcanism Program (GVP) database (Venzke, 2013) from 1800 to 2020 Appendix A; drives the “non-ENSO” Walker Circulation; is the largest area of tropical convection in the world; drives the northern and southern regional Hadley Circulation; covers the eastern part of the Indian Ocean used to calculate the IOD; and in recent decades has hosted one of the eight extreme, anthropogenic, continental scale, aerosol plumes from September to November (SON) Appendix B.

ENSO is the dominant interannual climate signal originating in the tropical Pacific and is driven by interactions between the atmosphere and ocean (McPhaden et al., 2006). It is defined in the Intergovernmental Panel on Climate Change (IPCC) Assessment Report Four (AR4) Glossary (Solomon et al., 2007) as a coupled atmosphere-ocean phenomenon with a two to seven year time scale with significant effects on the climate in the Pacific region and across the world.

ENSO events commence when the Trade Winds (TWs) blowing from east to west across the Pacific Ocean weaken (Enfield (1989), McPhaden et al. (1998), Brown and Fedorov (2010), Cai et al. (2015) and B. Wang and An (2002)). It is therefore clear that the TWs and therefore the Walker Circulation are intimately connected with ENSO events and determining the cause of the weakening of the TWs and Walker Circulation may well reveal the cause of ENSO events. It is known that aerosol plumes can alter the major atmospheric circulation systems (Solomon et al., 2007), (Remer et al., 2009) and the South East Asian aerosol Plume (SEAP) is uniquely positioned to influence the Walker Circulation as it, and only it, of the eight continental scale aerosol plumes exists in the region of non-ENSO Walker Circulation convection.

The literature includes many attempts to connect volcanic eruptions and ENSO events. Neville Nicholls (1988) and N. Nicholls (1990) investigated volcanic eruptions and El Niño events and concluded there was no connection. Hirono (1988) investigated the possibility that the 1983 eruption of El Chichon in Mexico could have triggered the El Niño which followed and Robock et al. (1995) investigating this hypothesis found that: the eruption did not trigger the El Niño event which followed; and that only trade wind collapses in the western Pacific Ocean can initiate ENSO events. Handler and Andsager (1990) investigated the volcanic hypothesis which states that low-latitude volcanic aerosols are the immediate and only cause of warmer than normal SST or El Niño and its inverse using Monte Carlo techniques and found that both aspects of the hypothesis were satisfied. Self et al. (1997) investigated volcanic aerosol perturbations and the 16 strongest El Niño events over the last 150 years and found no general correlation. In discussing the evolution of ENSO events Trenberth et al. (2002) suggested that the effects of volcanic eruptions on ENSO events remained unanswered questions. Emile-Geay et al. (2008) focused on very large eruptions which were greater than the Pinatubo eruption in 1991 and found that small eruptions have no effect. Zhang et al. (2013) investigated the effects of large eruptions using Aerosol Optical Depth (AOD) in latitudinal bands 0 to 30 and 30 to 90 in both hemispheres to force the climate model but did not consider the location or the intensity of the eruption and noted this should be done in the future. Cane (2005) reviewed forecasts of ENSO activity, found that there was no clear picture and suggested solar and volcanic variations in solar insolation and atmospheric aerosols might have a role. Ammann et al. (2003) found that including an improved volcanic eruption dataset in climate model simulations improved the correlation between the modelled data and observations whilst Mann et al. (2005) showed a short term response of ENSO to tropical eruptions. Other publications which address the link between volcanic eruptions and ENSO are Timmreck (2012), Maher et al. (2015), Blake et al. (2018) and Predybaylo et al. (2017).

There is therefore obviously great interest in, but no general agreement on, the connection between volcanic eruptions and ENSO events for two reasons: In general, only large eruptions were considered and smaller eruptions which do not eject tephra into the stratosphere were ignored; and a global analysis was undertaken rather than focusing on a specific region, south east Asia, which is the only area which can create and sustain an ENSO event because it is the region which drives the entire non-ENSO Walker Circulation. This paper provides the definitive explanation for the causation of ENSO events by volcanic eruptions by specifically focusing on eruptions within south east Asia and shows the same volcanic aerosols also create IOD events and drought in south eastern Australia.

2 Methods and Overview

I demonstrate that volcanoes in SEAsia have always created and sustained ENSO events in three stages by showing:

First that volcanic tephra from the SEAsian eruptions has a statistically significant connection to the three ENSO indices, Nino 3.4 and 1+2 SST, the SOI, and other ENSO related events using GVP data;

Second that aerosols over SEAsia are intimately connected to the three ENSO indices, using the Last Millennium Ensemble (LME) (Otto-Bliesner et al., 2016), MERRA-2 (M2) (Gelaro et al., 2017) and the NASA Terra/MODIS (Kaufman et al., 2000) and NCEP-R1 (Kalnay et al., 1996) (together TN) data; and

Third that the connection must flow from the aerosols to ENSO.

ENSO events are created in the following sequential stages:

1. The SEAP is established;
2. The SEAP aerosols absorb (and reflect) solar radiation which: (a) heats the atmosphere; and (b) reduces solar radiation at the surface under the plume which cools the surface; this
3. Creates a temperature inversion compared to times without a plume which reduces convection;
4. Reduced convection over SEAsia causes the TWs blowing from east to west over the Pacific Ocean as part of the Walker Circulation to reduce in intensity as there is a reduced exit into the convection and the Walker/Hadley Circulation;
5. Reduced TW speed over the Pacific Ocean causes the sea surface temperature to rise; which
6. Creates convection in this region and the Walker circulation further relaxes or even reverses;
7. The SOI is forced into a negative phase by these changes in convection;
8. The western Pacific warm pool then migrates east as the wind stress on the ocean has reduced;
9. The ENSO event continues until the aerosol plume over SEAsia dissipates which is typically when the SEAsian monsoon starts in mid November and washes the aerosols out of the atmosphere; and
10. With the revived TW speed over the Pacific Ocean the warm pool then migrates west again and the ENSO event ends.

This paper follows this sequence to establish the connection between each step and the SEAP and a schematic showing the development of an ENSO event is included in Appendix C.

2.1 Areas Used

The areas used in this analysis are shown in Fig. 1 and are:

1. The area covered by the SEAP (SEAP Area) 10º S-10º N and 90º E-160º E;
2. The Central SEAP (CSEAP) Area 5º S-5º N and 100º E-120º E;
3. The IOD Areas 50E-70E and 10S-10N and 90E-110E and 10S-0N
4. SEAus pressure 130º to 145º E and 25º to 40º S and Melbourne;
5. SEAus rainfall 137º to 160º E and 30º to 40º S and Melbourne;

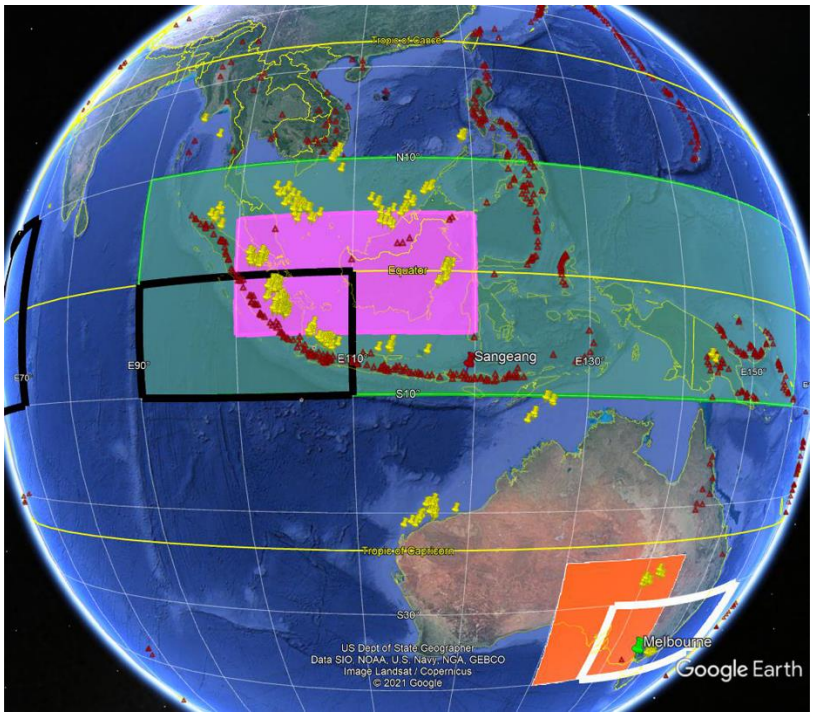

Figure 1. The SEAP Area, green; CSEAP Area, pink; IOD Areas, black outline; SEAus pressure, orange; SEAus rainfall, white outline; Melbourne, green pin; volcano locations from the GVP in red; and gas flares (NOAA and the Global Gas Flaring Reduction Partnership (GGFRP), yellow. Map data: Google Earth, US Dept of State Geographer, SIO, NOAA, U.S. Navy NGA, GEBCO; image Landsat/Copernicus. © **Google Maps 2021**.

2.2 ENSO Theory, Models and Climate Models

Since Bjerknes (1969) first described the link between the atmospheric and oceanic components of ENSO events several theories have been developed to explain the triggering, development and decay of ENSO events. Bjerknes (1969) suggested that the ocean triggered ENSO events with the warmer SST creating convection in the central Pacific Ocean and slowing the Walker Circulation which created higher pressure in Djakarta/Singapore. However, this is at odds with the literature cited above which clearly states that relaxation of the Trade Winds triggers ENSO events. Kleeman and Moore (1997) suggest that the predictability of ENSO events is limited by the stochastic forcing of atmospheric transients and this is in accord with this paper which shows the atmospheric transients are created by the volcanic SEAP which is inherently unpredictable. Zebiak and Cane (1987) proposed a simple coupled atmosphere/ocean ENSO model which demonstrated oscillatory behaviour with a period of 3 to 4 years and stated that this oscillation is

an internal characteristic of the coupled system as, apart from year one there is no external forcing. This implies that the recurrence of ENSO in the LME data at a similar period across eight significantly different forcing scenarios is also an internal characteristic of the model. One inherent characteristic of ENSO events is their synchronisation to the annual cycle and Stein et al. (2014) suggest this is due to annual modulation of the coupled system. This paper shows that the annual modulation is driven by the south east Asian monsoon which clears aerosols from the SEAP Area allowing convection and the TWs to be re-established and the oceanic elements of ENSO to relax back to their non-ENSO state over the following months. Dijkstra (2006) found that the internal variability and feedbacks within the coupled atmosphere/ocean system create ENSO events, whilst acknowledging that the mechanism which creates ENSO irregularity has not yet been identified which is exactly what this paper does.

C. Wang (2018) reviewed the theories used to model ENSO and categorised them as: (1) a stable mode interacting with high frequency forcing (HFF); and (2) a self-sustaining oscillation which was split into four types: delayed; recharge-discharge; western Pacific; and advective-reflective. The paper concludes that there is no agreement yet on which category is correct.

This paper: supports (Kleeman & Moore, 1997) and (Dijkstra, 2006); demonstrates that the high frequency forcing is the volcanic tephra over SEAsia; and therefore shows that the category (1) HFF theory in C. Wang (2018) is correct.

Khodri et al. (2017) using data from the Fifth Coupled Model Intercomparison Project (CMIP5) found that volcanically induced cooling of tropical Africa drives equatorial wind anomalies in the central Pacific Ocean which tends to favour an ENSO like response within two years. However, the progression from an African eruption, which is remote from the Walker Circulation and ENSO centres, Nino 3.4 and 1+2 and the SOI centres of Darwin and Tahiti, to an ENSO event is complex involving atmospheric Kelvin waves and relies on a latency within the climate to create an ENSO event within two years. Fadnavis et al. (2021) investigated the effects of the Nabro volcanic eruption in north east Africa in 2011 on the Indian summer monsoon and noted that, using the complex methodology described in Khodri et al. (2017), the eruption induced warming in the central Pacific Ocean, whereas this paper provides a simple and immediate explanation for the triggering and sustaining of ENSO events by volcanic eruptions in south east Asia which is within the Walker Circulation and ENSO centres.

It should be clearly understood that Climate Models are “tuned” to produce, inter alia, the required ENSO characteristics and this is how climate models produce ENSO events without volcanic forcing. For confirmation see Hourdin et al. (2017), Mignot et al. (2021), Schmidt et al. (2017) and Senior et al. (2020). Hence climate models produce ENSO events with the expected characteristics because they are tuned to do so and until the tuning process creates the required characteristic tuning continues. One of the cited papers suggests that the tuning process is the most time-consuming process confronted in the development of a climate model and takes up to 3 years.

The climate models used in CMIP6 have been assessed for “ENSO Performance” in the Historical Experiment (HE) using Planton et al. (2021) which lists four segments of metrics: Climatology (8); Basic Characteristics (7); Teleconnections (4); and Processes (5). However, no metric assesses the accurate reproduction of the sequence of known ENSO events in the HE!

2.3 ENSO and volcanic eruptions

The anthropogenic SEAP has only existed in its current form since about 1980 (Fig. 2 which shows a 500% increase from 1980 to 2000 and Appendix B) and as ENSO events have most likely occurred for millions of years (NOAA at https://www.pmel.noaa.gov/elnino/faq) the driver of historic ENSO events must be the natural SEAP created by volcanic eruptions Appendix A and, according to the Volcano Global Risk Identification and Analysis Project at https://www2.bgs.ac.uk/vogripa/index.cfm and the Global Volcanism Program at https://volcano.si.edu/volcano.cfm?vn=261090 SEAP Area volcanoes have been erupting for the same period e.g. Toba's earliest eruption is dated at 1.2 Ma.

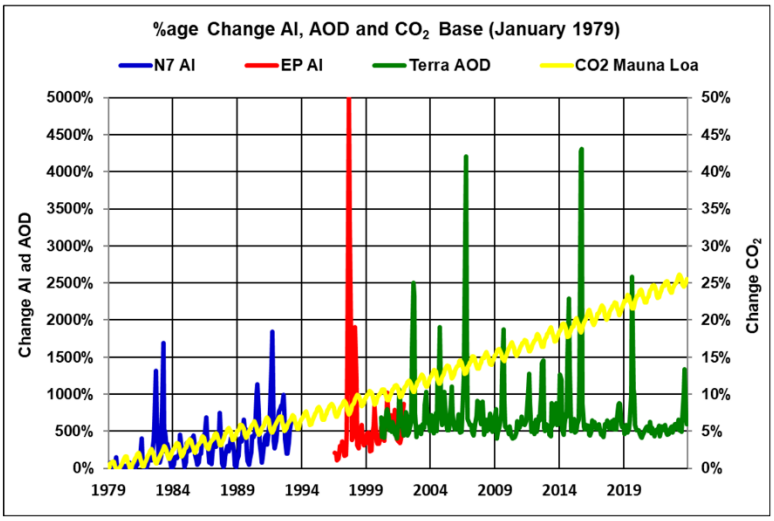

Figure 2. Percentage change in: monthly average CSEAP Area, Aerosol Index (AI) (TOMS instrument - Nimbus 7 (N7); Earth Probe (EP); and AOD (Terra) with the Mauna Loa CO_2 (Keeling et al., 2005). Note: (1) the vertical scales differ by two orders of magnitude; (2) the near random occurrence of significant peaks; and (3) the increasing trend in AI from 1979 to 2000.

2.4 ENSO seasonality, character and return frequency

The literature describes ENSO events as exhibiting a return frequency of two to seven to ten years and the University Corporation for Atmospheric Research (UCAR) website at http://webext.cgd.ucar.edu/Multi-Case/CVDP_repository/cesm1.lm/nino34.powspec.png shows the ENSO power spectra for all the LME runs and the same information for the HadISST_1 (Rayner et al., 2003) and ERSST v5_1 (Huang et al., 2017). The HadISST_1 and ERSST v5_1 spectra are similar and Fig. 3(a) shows the multiple peaks in the HadISST_1 data whilst all the LME runs show a single peak at about 5 years e.g., Fig. 3(b), and are nearly identical even with the different forcings used and are all very different from the measured spectra. I suggest that the reason for the difference is that none of the forcings applied in the LME runs included volcanic forcing at the required spatial and temporal resolution and this is discussed later.

The combination of HadlSST_1 and SEAP Area volcanic tephra power spectra from 1980 to 2017 in Fig. 3(c) shows that the SEAP Area volcanic tephra power spectrum is similar in form to the HadlSST_1 spectrum with nearly identical multiple peaks including the major peaks at 6.17 and 5.42 years respectively. Given the uncertainties in the tephra data which is based on GVP Volcanic Explosivity Index (VEI) data available as integer values on a pseudo logarithmic scale and converted to tephra (VEIT) using Table 1 in (Newhall & Self, 1982), the similarity of the spectra is impressive.

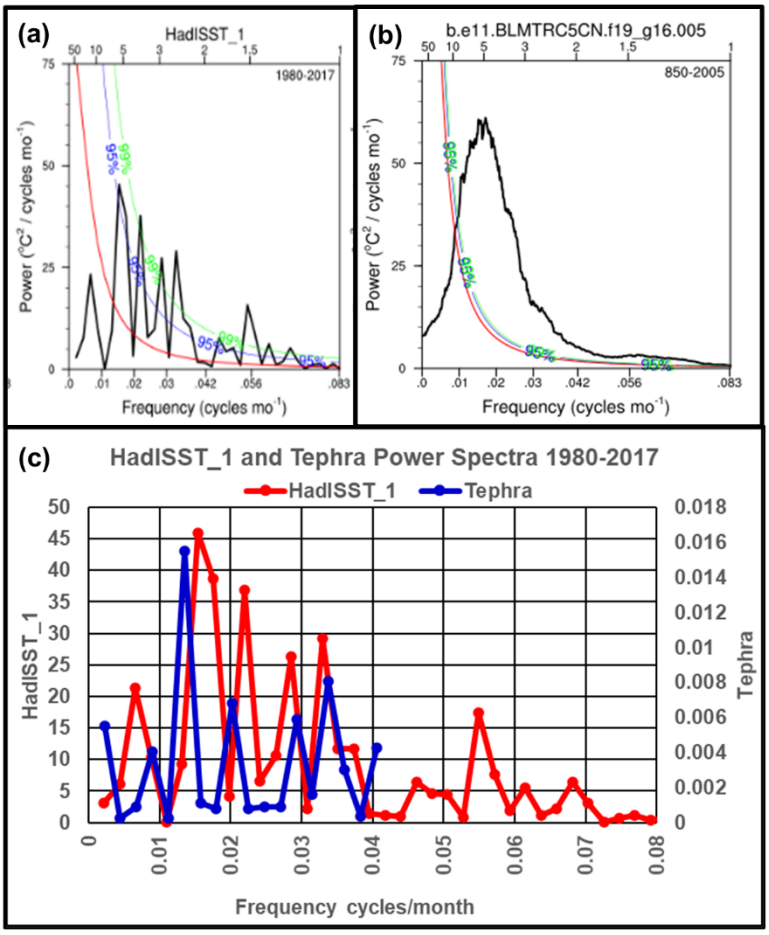

Figure 3: ENSO power spectra: HadISST_1 (a); LME all forcings run 5 (b); and combined HadlSST_1 and SEAP Area tephra (c).

ENSO is highly seasonal as Fig. 4 shows and this paper provides an explanation for the seasonality. NCEP/NCAR average monthly rainfall in the CSEAP area and the Nino 3.4 SST (1980-2020) correlate at -0.57 significance <0.1 with the SST reducing when rainfall in the CSEAP Area is high. This clearly supports the hypothesis that the SEAP is the cause of ENSO events as the SEAsian monsoon rainfall washes the aerosols out of the atmosphere in the SEAP Area enabling convection to be re-established in the region to drive the TWs and end the ENSO event.

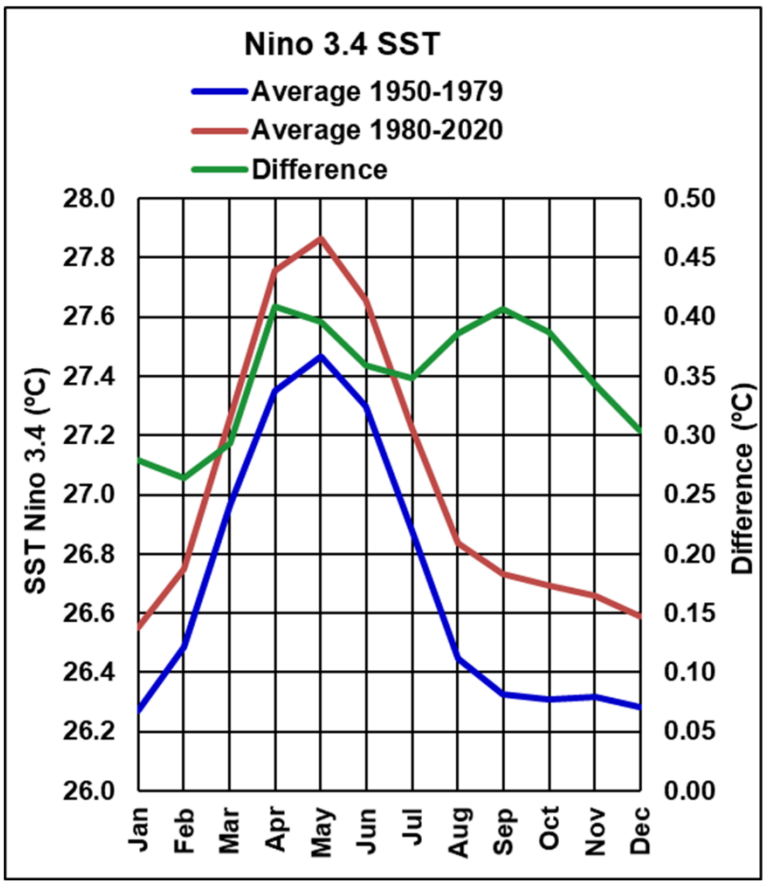

Figure 4: NCEP-R1 Reanalysis Nino 3.4 SST averages: 1950-79; 1980-2020; and the difference. Source NCEP Reanalysis

ENSO has become more intense in recent decades as Fig. 4 demonstrates with the Nino 3.4 SST rising by over 0.25°C in recent decades and especially in Aug-Nov when the anthropogenic SEAP is at its peak. This change in ENSO is noted in the IPCC AR6 Working Group 1 Draft Report at 2-97 (48-51) relying on Grothe et al. (2020) who state that in the recent five decades ENSO activity is 25% stronger than in the preindustrial era.

The general rise in all months is due to the increase in the levels of both the natural and anthropogenic SEAP as Appendices A and B and Fig. 2 show and the anomalous rise from Aug to Nov is entirely due to the extreme apparitions of the anthropogenic SEAP.

2.5 Walker Circulation

The Walker Circulation is defined in the IPCC AR4 Glossary as a direct thermally driven zonal atmospheric circulation over the tropical Pacific Ocean, with convection in the west and sinking air in the east (See also C. Wang (2002), Barry and Chorley (2010), Trenberth et al. (2000) and Sturman and Tapper (1996)).

The Australian Bureau of Meteorology (BOM) shows images of the atmospheric circulation during El Niño, La Nina and neutral seasons on its website at:

http://www.bom.gov.au/climate/about/australian-climate-influences.shtml?bookmark=enso. It is clear from these figures that the "direct thermal drive" for the La Niña and neutral Walker Circulation must be located at ground level in the SEAP Area where solar radiation heats the Earth's surface which in turn heats the atmosphere as the rising limb of the non-ENSO Walker Circulation is located there in exactly the same location as the SEAP which is therefore uniquely positioned to directly affect the Walker Circulation and create ENSO events.

Since variations in the solar energy at the top of the atmosphere cannot explain the reduction in the surface heating in the SEAP Area which causes convection and the Walker Circulation to relax, the reduction must be caused by variations within the atmosphere where the SEAP reduces surface solar radiation. Indeed: Tosca et al. (2015) investigated the effects of anthropogenic aerosols in West Africa and reported that anthropogenic aerosols in the tropics limit convection; and Fig. 2.23 ((Nozawa et al., 2005) and (Takemura et al., 2005) in chapter 2 of the IPCC AR4 shows that, on a globally averaged basis, surface radiative forcing is controlled by aerosols with the net effect of long-lived greenhouse gases, ozone, aerosols and land use aligning nearly perfectly with the aerosol direct effect.

Therefore, from the IPCC AR4 and literature it is a plausible hypothesis that the SEAP could force the Walker Circulation and TWs to relax by reducing the surface solar radiation available to drive convection in the SEAP Area.

2.6 The Indian Ocean Dipole and ENSO

The IOD (Saji et al., 1999) is described on the BOM website at http://www.bom.gov.au/climate/iod/ which shows images of the Indian Ocean atmospheric circulation in the three phases of the IOD and states that: IOD events start in May/June; peak a few months later and decay at the end of the southern spring when the monsoon arrives in the southern hemisphere. The BOM images clearly show that convection reverses over the SEAP Area when the IOD moves from a negative/neutral to positive phase.

Abram et al. (2020) found a persistent coupling has existed between the variability of the IOD and the El Niño Southern Oscillation during the last millennium and the BOM website shows that the relaxing/reversing of convection in the SEAP Area is common to both. I show that the SEAP, uniquely positioned to control convection in the SEAP Area, drives both events simultaneously.

2.7 South Eastern Australia rainfall

Drought in SEAus has a major effect on agriculture and has been linked to ENSO and the IOD. The Centre for Australian Climate and Weather Research (CAWCR) produced technical report 26 (Timbal et al., 2010) which found the major agents correlating with drought are ENSO and higher Mean Sea Level Pressure (MSLP) in SEAus in the southern Autumn, Winter and Spring, whilst Ummenhofer et al. (2009) state that it is the IOD and not ENSO which drives drought in SEAus. I show that MSLP increases over SEAus from April to October, the wet season in SEAus, are driven by the SEAP perturbing the southern regional Hadley Circulation by forcing the associated tropical convection and sub-tropical high to the south. Thus, I show the SEAP simultaneously creates ENSO and IOD events and drought in SEAus.

2.8 Global Temperature

It is well known that the global temperature increases during an ENSO event. The Hadley Centre CRUTEM5 global temperature dataset (Morice et al., 2021) shows that the average annual global temperature increases by over 0.3ºC during an ENSO event with some months showing increases of over 0.7ºC. Hence it is essential to show, contrary to accepted science that aerosols cool the World, that the SEAP causes the World to warm if it is indeed the cause of ENSO events. The results section shows that: on average across the eight LME simulations the annual global temperature rises by 0.65ºC from minimum to maximum SEAP AOD, and the trend maps from all the eight LME simulations analysed show that whilst the SEAP reduces surface temperatures under the plume the remainder of the World warms significantly.

2.9 The South East Asian aerosol Plume (SEAP)

This paper focuses on SEAsia as this region is where convection, which drives the Walker Circulation, occurs and is therefore where aerosols can have a significant effect. Appendices A and B describe in detail the sources of aerosols in the SEAP Area, the natural SEAP derived from volcanic eruptions and the anthropogenic SEAP derived mainly from biomass burning and gas flares in the oil production industry. Reid et al. (2013) provides a review of the south east Asian aerosol system.

2.9.1 The natural SEAP

The SEAP Area, which covers about 3.4% of the globe, is the world's most tectonically active area with the United States Geological Survey (USGS) earthquake database (USGS, 2021) showing 25% (5 of 20) of the major earthquakes (magnitude > 8.4) in the world since 1900 occurred in the SEAP Area and the GVP database showing that from 1800 to 2020 over 26% of the global volcanic eruptions occurred in the SEAP Area (Appendix A). Simkin and Siebert (2000) state that 5 of 16 (31%) of the continuously erupting volcanoes in the world for the past 24 years are located in the SEAP Area and that one more, in Vanuatu, is just to the south east of the SEAP Area.

Note: The SEAP is the only one of the eight continental scale aerosol plumes (Appendix B) which contains such significant levels of volcanic aerosols.

2.9.2 The anthropogenic SEAP

The anthropogenic SEAP is one of eight continental scale, anthropogenic, aerosol plumes which occur annually and are shown in Appendix B. These extreme plumes typically exist for a few months each year at the end of the regional dry season when biomass burning can occur. The SEAP is easily identified on the monthly mean AOD and AI data. The change in the CSEAP Area AI and AOD is shown in Fig. 2 and was extremely high in 1982, 1983, 1991, 1997, 2002, 2004, 2006, 2009, 2014, 2015 and 2019 compared with the intervening years. 1983 is the only year where an extreme peak emission is not in September or October. The Terra AOD data is shown in greater detail in Appendix B to demonstrate clearly the peak anthropogenic aerosol emission season is SON, the end of the dry season in SEAsia.

CALIPSO (Cloud-Aerosol Lidar and Infrared Pathfinder Satellite Observations) (Winker et al., 2009) profiles confirm a layer of smoke existed at about 3Km altitude in October 2015 in the SEAP Area and Fig. 5 shows the geographic extent of the 2015 extreme apparition of the SEAP. This paper analyses the effects of the SEAP on an annual and SON (when the anthropogenic plume is most intense and therefore has its greatest effect) basis.

The maximum SEAP AOD was 1.60 (Oct 2015) and the maximum Nimbus 7 (N7) and Earth Probe (EP) AI was 1.81 (Sept 1997). The AI of the CSEAP Area increased by about 500% from Jan 1979 to 1992 and by slightly more in 2000 in years without extensive biomass burning. From Jan 1979 to Sep 1997, a major biomass burning event year (Applegate et al., 2001), the increase in September AI was 5,000%. Note the AI and AOD in 2000/01 are the same magnitude and the AOD percentage increase has been calculated on this basis.

The surface radiative forcing of the anthropogenic SEAP is significant and the literature includes:

1. A 10% to 30% reduction of Photosynthetically Active Radiation (Ramanathan, 2006);
2. -150 W m-2 (Duncan et al., 2003); and during ACE-Asia, ~-286.0 W/m2/τα (Hansell et al., 2003).
3. Figure 7 in Ott et al. (2010) shows the atmospheric heating effect of the SEAP in 2006 with temperature rises of over 0.5º C in October from 400 to 200 hPa.

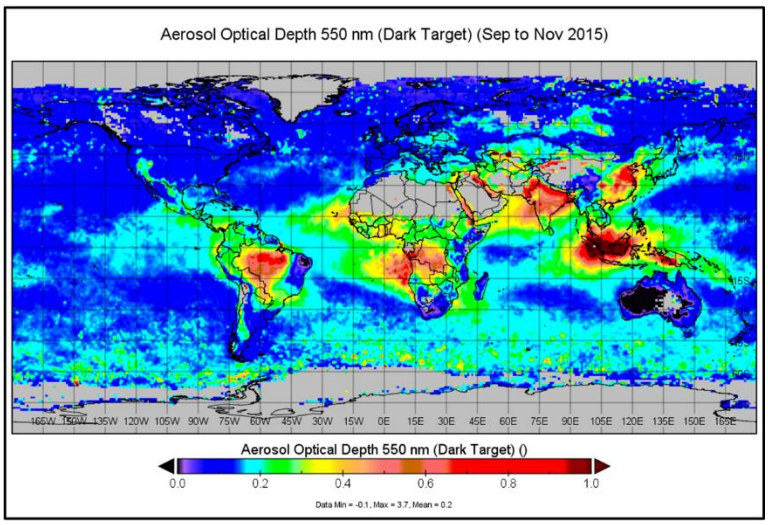

Figure 5. NASA Terra/MODIS AOD in SON 2015. Source: NASA Giovanni.

2.9.3 The SEAP in the LME and MERRA-2

It is worth noting here that the AOD in both the LME and M2 data is far too low and this problem is discussed later.

3 DATA

The creation of ENSO events by the natural and anthropogenic SEAP is demonstrated by showing that each step in the development of an ENSO event outlined above is directly linked to the SEAP in three ways:

First: the GVP data is used to demonstrate a direct link from the tephra ejected by volcanoes in the SEAP Area to the ENSO indices and other associated events;

Second: modelling, reanalysis and satellite data is used to show the same effects as tephra and that ENSO and associated events can all be explained by physical mechanisms controlled by the SEAP;

Third: The LME annual data from the eight simulations is used to create trend maps of the parameter being analysed. The trend maps are created by:

1. Computing the trend line equation of the SEAP AOD and the parameter being analysed at each point on the map;
2. Computing the values of the parameter at the minimum and maximum SEAP AOD values and the difference between them;
3. Plotting the differences as a map;
4. Computing the correlation of the SEAP AOD and the parameter and the Student's t value;
5. Plotting the t values of 0, 2.59, 3.31 and 3.92 which correspond to significance levels of 0 (change from negative to positive correlation) 0.01, 0.001 and 0.0001 on the same map as a contour;

3.1 Volcano data

Volcanic eruption tephra was derived from the GVP database using only confirmed eruptions, calculated as shown in Appendix D and analysed using the segments in Table 1. The other parameters used were: the NOAA ENSO indices (Nino 3.4 and 1+2 SST); BOM SOI; NCEP-R1 reanalysis SST, omega and wind speed; BOM 9:00am sea level pressure and rainfall for south eastern Australia; and the NOAA Dipole Mode Index (IOD) and these datasets limited the time span of the analysis to the periods in Table 1.

This data was not detrended due to the massive eruptions of Krakatau (1883) and Agung (1963) distorting the detrending process.

		GVP Data Segments (Km^3)	Period
1	Surface Temp SEAP Area	Standard	1948-2020
2	Omega SEAP Area	Standard	1948-2020
3	Wind Speed Nino 3.4 Area	Standard	1948-2020
4	Nino 3.4 SST	Standard	1870-2020
5	Nino 1+2 SST	0, 0.00054, 0.001, 0.004, >0.004	1870- 2020

6	SOI	Standard	1876-2020
7	Convection Nino 3.4 Area	0, 0.007, 0.02, > 0.02	1948-2020
8	IOD (May to October)	Standard	1870-2020
9	Pressure SE Australia (Apr-Oct)	0, 0.00035, 0.0004,0.001, 0.01, >0.01	1903-2020
10	Rainfall SE Australia (Apr-Oct)	0, 0.0003, 0.0005, 0.001, 0.005, 0.1, > 0.1	1870-2020
11	Global annual temperature	0, 0.0001, 0.001, 0.01, 0.015, >0.015	1870-2020

Table 1. GVP volcano data segments and analysis periods. Standard segment boundaries are 0, 0.0001, 0.001, 0.01, 0.1 and greater than 0.1 Km^3. Periods other than 1870-2020 are limited by the availability of BOM data except for 1948-2020 which is limited by the NCEP-R1 reanalysis data.

3.2 Modelling, reanalysis and satellite data

All this data was detrended by: copying all the individual time series (88 for the LME, 11 for M2 and 22 for TN (annual + SON)) to PAST 3 (Hammer et al., 2001), a statistical analysis software package; detrending the data (a simple one-click process); copying the detrended data back to a spreadsheet; and adding the average of the un-detrended data to each element of the time series to give a series with the same average magnitude as the un-detrended data which enables a direct comparison between measured data and the LME, M2 and TN data.

3.2.1 Last Millennium Ensemble (LME)

The LME data analysed is: atmosphere, post processed monthly averages consisting of seven simulations (Table 1 (Otto-Bliesner et al., 2016)) plus “850” which were repeated in multiple runs. Aerosol Optical Depth (AOD) (AODVIS), surface pressure (PSL), surface temperature (TS), precipitation (PRECL), vertical pressure velocity (OMEGA) and wind speed (U10) data from these simulations(run) was downloaded: (850 (3); All (13); Ozone and Aerosol (2); Green House Gas (3); Land Use (3); Orbital (3); Solar (5); and Volcanic (5). Each simulation(run) provided two NetCDF data files for each parameter covering the entire world from 850 to 1849 and 1850 to 2005 except for the ozone and aerosol simulation which provided one file from 1850 to 2005. Matlab (Matlab, 2019) was then used to: extract data for the required areas from each file; create a single time series of 1,156 years (13,872 months); and export the time series data and date together with the latitudes and longitudes used to a spreadsheet.

The time series data was then converted to tabular form by year and month, checked for accuracy by summation of the time series and table, and the average (total for rainfall) annual data calculated. This data was then detrended as described above. Finally, data for each parameter from all eight simulations/runs was plotted on the same scatter plot against the AOD for the same simulation/run to give 8,248 points, the trend and R^2 value and on a second scatter plot with the individual simulations separated on the AOD axis by 0.1.

Climate indices for the IOD and SOI are not available directly from the LME. The IOD was calculated using TS from the standard IOD areas. The SOI was calculated using the BOM

formula at: http://www.bom.gov.au/climate/enso/soi/about-soi.html and PSL data for the areas near Darwin (12º to 14º S and 130º to 133º E) and Tahiti (16º to 18º S and 207º to 213º E).

Note:

(1) TS (skin temperature) from the atmosphere dataset was used rather than SST (sea surface temperature) from the ocean dataset for simplicity as the ocean dataset is provided on a rotated grid rather than latitude and longitude.

(2) Although the annual LME SEAP Area AODVIS data ranges from 0.04 to 0.11 which is significantly lower than the Terra annual data which ranges from 0.18 to 0.27, the data still shows statistically significant relationships between the SEAP Area AOD, the ENSO indices and the other parameters.

(3) The volcanic forcing data in the LME cannot of itself demonstrate the connection between the natural volcanic SEAP and ENSO as it does not have the resolution required to do so. It is derived from ice cores in the Arctic and Antarctic (Otto-Bliesner et al., 2016) and Gao et al. (2008) who provide the data as only stratospheric sulphate forcing in latitude bands (ten degrees wide), by altitude and month. For volcanic tephra to travel to the polar regions the tephra must be injected into the stratosphere requiring a minimum VEI of 3 to 4. Hence all the VEI 0,1,2 and some (50% assumed) of the VEI 3 eruptions in the SEAP Area must be missing from the dataset. Since this excludes over 98% of the eruptions in the SEAP Area since 1870 which are used in this paper the resolution of this LME volcanic forcing dataset is inadequate in itself in terms of eruption size, geo-space, time and aerosol type to prove the causation of ENSO by SEAP Area volcanic tephra described in this paper. However, the LME volcanic forcing does provide another independent aerosol forcing dataset which shows the same results as the other LME simulations and is therefore included in the analysis.

3.2.2 MERRA-2 reanalysis

A similar approach was used for the NASA M2 reanalysis dataset (1980-2020) which includes assimilated aerosols. AOD (M2IMNXGAS_5_12_4_AODANA), surface pressure (M2IMNPANA_5_12_4_PS) precipitation (M2TMNXFLX_5_12_4_PRECTOT) surface skin temperature (M2TMNXSLV_5_12_4_TS), omega (M2IMNPASM_5_12_4_OMEGA) and surface eastward wind (mean_M2TMNXFLX_5_12_4_ULML) data was downloaded, and annual averages or totals calculated. All M2 data was detrended in the same way as the LME data.

The SOI and IOD for the M2 analysis were calculated using data from the M2 dataset using the BOM formula for the SOI and surface pressure near Darwin (130º to 131º E and 12º to 13º S) and Tahiti (149º to 150º W and 17º to 18º S) and TS for the standard IOD areas.

3.2.3 Satellite data

AOD data from the Terra satellite (2000-2020) for the SEAP Area was downloaded together with the NCEP-R1 reanalysis sea surface temperature (SST), omega, sea level pressure, precipitation rate and zonal wind. Annual and SON time series were calculated for all these parameters and the NOAA Nino 3.4 and 1+2 SST, the BOM SOI and the NOAA IOD. The SON data is used to show the significant effect the extreme anthropogenic SEAP has in SON.

3.3 Data sources

LME:	https://www.earthsystemgrid.org/dataset/ucar.cgd.ccsm4.CESM_CAM5_LME.html
MERRA-2:	https://giovanni.gsfc.nasa.gov/giovanni/
GVP	https://volcano.si.edu/list_volcano_holocene.cfm
Terra	https://giovanni.gsfc.nasa.gov/giovanni/
NCEP:	https://psl.noaa.gov/cgi-bin/data/timeseries/timeseries1.pl
SST	Niño 3.4 area (5º S-5º N, 170º W-120º W) and Nino 1+2 areas (10°S–0°, 90°W–80°W). http://www.cpc.ncep.noaa.gov/data/indices/
SOI	http://www.bom.gov.au/climate/current/soihtm1.shtml
ENSO Indices	https://psl.noaa.gov/gcos_wgsp/Timeseries/
IOD	https://psl.noaa.gov/gcos_wgsp/Timeseries/DMI/
Omega	(vertical motion in the atmosphere) at 600mb level - CSEAP Area. http://www.esrl.noaa.gov/psd/cgi-bin/data/timeseries/timeseries1.pl (Source 1)
SST SEAP Area	(Source 1)
TW Index (TWI)	(850mb at 5º N-5º S, 175º W-140º W) http://www.cpc.ncep.noaa.gov/data/indices/cpac850 (Source 2)

Pressure and rainfall SEAus: BOM climate data cd to 2010 and Source 1

4 RESULTS

Results: are shown in the order of the sequence of events required to create an ENSO event outlined in the methods section; the specific stage is noted in the title; and are presented as:

1. Scatter plots of the segmented volcano data with the volcanic tephra shown on a logarithmic scale. The segment boundaries used are listed in Table 1;
2. Scatter plots of the LME, M2 and TN annual and SON data which demonstrate the effects of the very high SEAP Area AOD in SON;
3. Scatter plots of the individual LME simulations to demonstrate there is little variation between the simulations and that the SEAP is the only forcing agent driving the changes;
4. Trend Maps for each of the eight LME simulations with the SEAP Area, Nino 3.4 and 1+2 areas, and the IOD areas highlighted; and
5. A listing of the correlations shown on the graphs in Table 2 with: change per unit AOD; change over tephra/AOD range; and percentage change in rainfall.

4.1 Stage 1: The SEAP forms

The 2015 SON SEAP AOD was at extreme levels and Fig. 6 shows the 2015/2016 comparison with Borneo and most of Sumatra, the CSEAP Area, covered by AOD increases over 1.0 and over half the SEAP Area showing increases over 0.2. It should also be noted that the SEAP AOD

as measured by Terra ranges from 0.175 to 0.266, average 0.207 whilst the LME data ranges from 0.036 to 0.111, average 0.055. The M2 SEAP AOD is also low compared to the TERRA data with the M2 data average being 66% of the TERRA average over the same period.

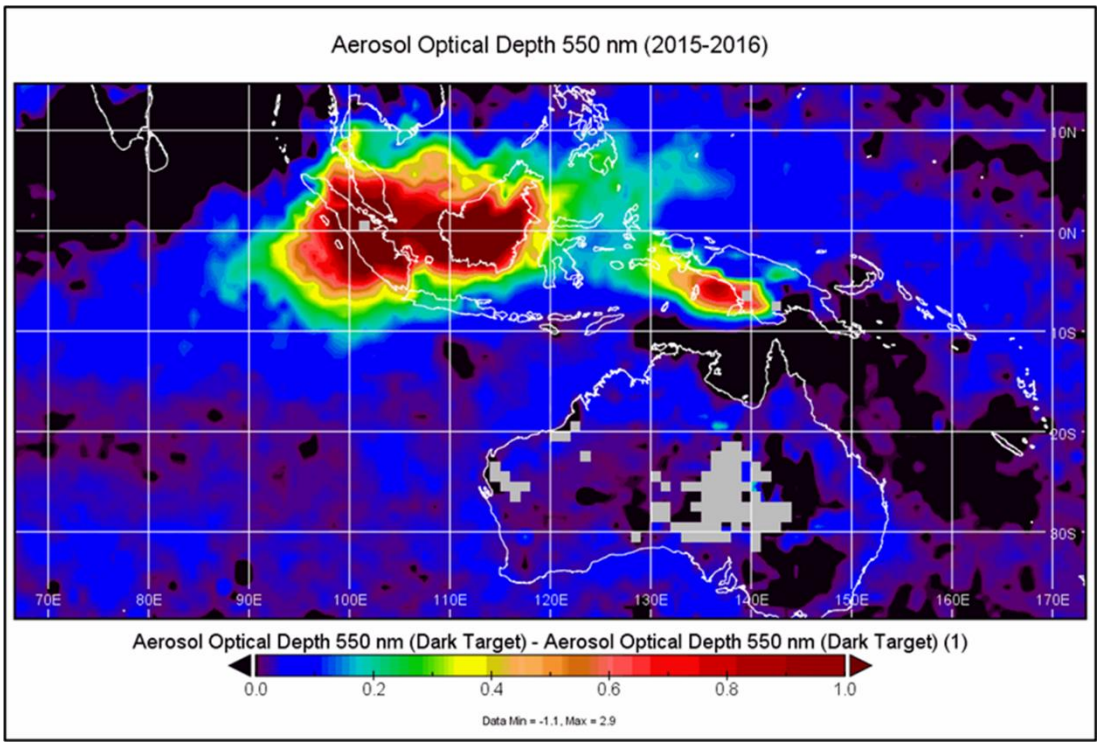

Figure 6. Terra/MODIS AOD SON 2015-2016 (Source NASA Giovanni and Panoply)

4.2 Stage 2(a): The SEAP warms the troposphere

Ott et al. (2010) investigated the extreme SEAP of Aug-Nov 2006 and Figures 6, 7 and 8 in the paper clearly show atmospheric heating due to the aerosols from 1,000 to 150 hPa.

4.3 Stage 2(b): The SEAP reduces surface solar radiation cooling the surface

Investigating the effects of the extreme 1997 biomass burning in Indonesia in SON Rajeev et al. (2008) found that this event caused surface radiative forcing of over -46W/m^2 and more than 1º C cooling of the surface. Table 1 shows that standard segments are used for the volcano data and Table 2 and Fig. 7(a) show that increasing levels of tephra result in a lower TS in the SEAP Area of up to 0.3ºK. Fig. 7(b) shows the changes in the SEAP Area TS with increasing SEAP AOD and Fig. 7(c) shows that all the individual LME simulations show the same result with an average reduction in the SEAP Area TS from minimum to maximum SEAP AOD of 0.72ºK. Fig. 7(c) also shows the average R^2 values across the eight individual simulations is 0.37 showing the SEAP controls 37% of the variation in the SEAP Area TS and is therefore forcing significant changes. Fig. 7(d) to (k) show the change in TS in the individual LME simulations, calculated as noted above, and show that on a global scale the agent driving the TS change is the SEAP as the structure of the change is identical in each trend map with only minor variations in the detail.

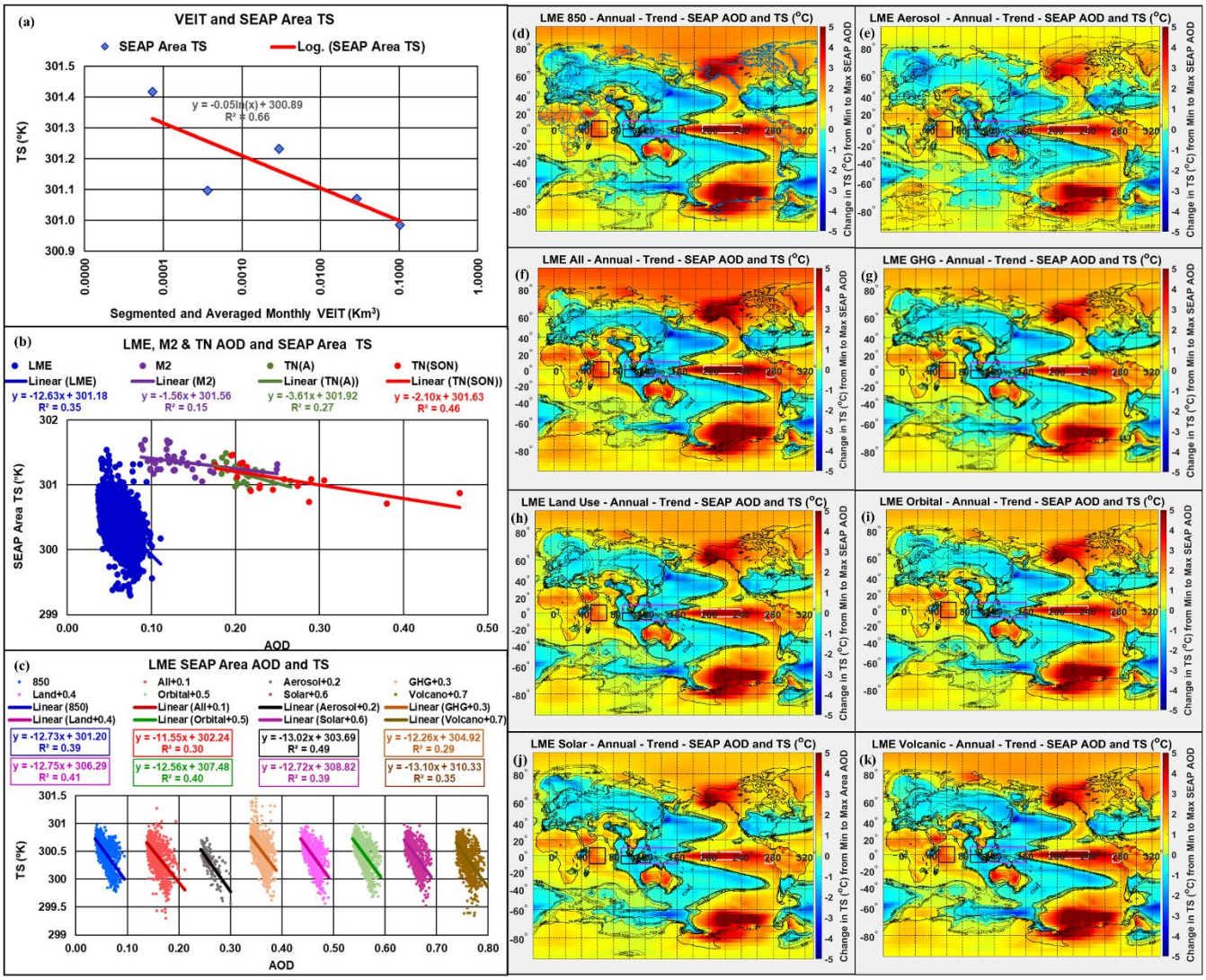

Figure 7. Scatter plots showing: segmented annual SEAP Area VEIT and TS (a); LME, M2 and TN annual and TN SON SEAP Area AOD and TS (b); Scatter plots of the individual LME simulations of annual SEAP Area AOD and TS separated by 0.1 along the AOD axis (c); and trend maps of the individual simulations named on the map titles (d) to (k)

4.4 Stage 3: Reduced SEAP Area SST reduces convection

Note: Omega is vertical pressure velocity in the atmosphere. Positive values indicate falling motion and negative values rising, and increased omega therefore means reduced convection.

Table 1 shows that standard segments are used for the volcano data and Table 2 and Fig. 8(a) show that increased levels of tephra result in increased omega and thus reduced convection in the SEAP Area. Fig. 8(b) shows the changes in the SEAP Area omega with increasing SEAP AOD and Fig. 8(c) shows that all the individual LME simulations show the same result with an average increase in the SEAP Area omega from minimum to maximum SEAP AOD of 0.028 hPa/s. Fig. 8(c) also shows the average R^2 values across the eight individual simulations is 0.68 showing the SEAP controls 68% of the variation in the SEAP Area omega and therefore is the

548 only agent forcing this major change. Fig. 8(d) to (k) show the change in omega in the individual
549 LME simulations, calculated as noted above, and show that on a global scale the agent driving
550 the omega change is the SEAP as the structure of the change is identical in each trend map with
551 only minor variations in the detail.

552

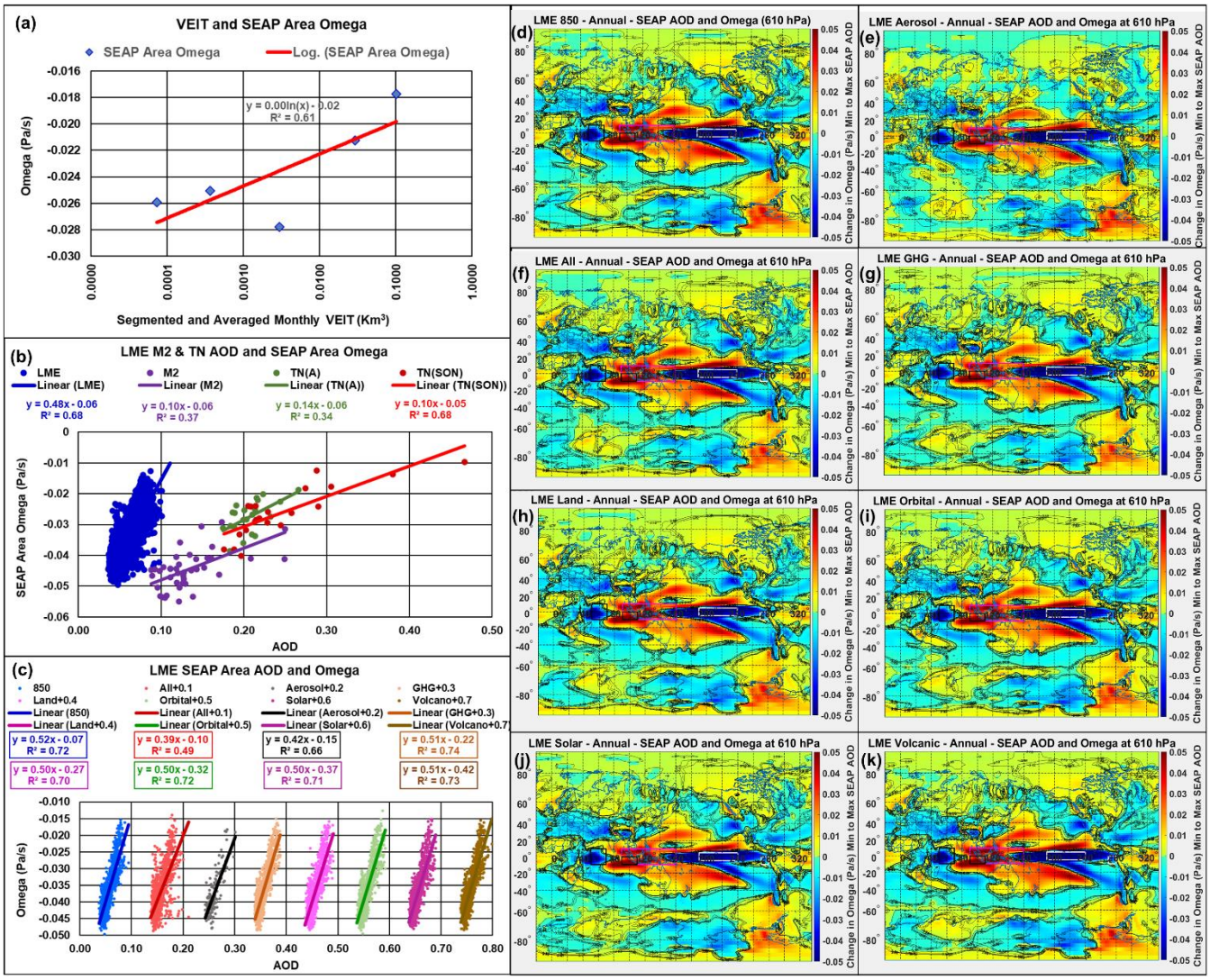

553

554 **Figure 8**. Scatter plots showing: segmented annual SEAP Area VEIT and omega (a); LME, M2
555 and TN annual and TN SON SEAP Area AOD and omega (b); Scatter plots of the individual
556 LME simulations SEAP Area AOD and omega separated by 0.1 along the AOD axis (c); and
557 trend maps of the individual simulations named on the map titles (d) to (k)

558 ### 4.5 Stage 4: Reduced convection in the SEAP Area causes the trade winds to relax

559 Table 1 shows the standard segments used for the volcano data and Table 2 and Fig. 9(a) show
560 that increased levels of tephra result in reduced TW velocity in the Nino 3.4 area. Fig. 9(b)
561 shows the changes in the TW velocity with increasing SEAP AOD and Fig. 9(c) shows that all
562 the individual LME simulations show the same result with an average reduction in the Nino 3.4

area TW velocity from minimum to maximum SEAP AOD of 2.15m/s. Fig. 9(c) also shows the average R^2 values across the eight individual simulations is 0.74 showing the SEAP controls 74% of the variation in the Nino 3.4 TW velocity and therefore is the only agent forcing major changes in the Nino 3.4 area TW velocity. Fig. 9(d) to (k) show the change in U10 velocity in the individual LME simulations, calculated as noted above, and show that on a global scale the agent driving the U10 velocity change is the SEAP as the structure of the change is identical in each trend map with only minor variations in the detail.

Note: wind direction has been aligned across the datasets and positive velocity denotes winds blowing from east to west.

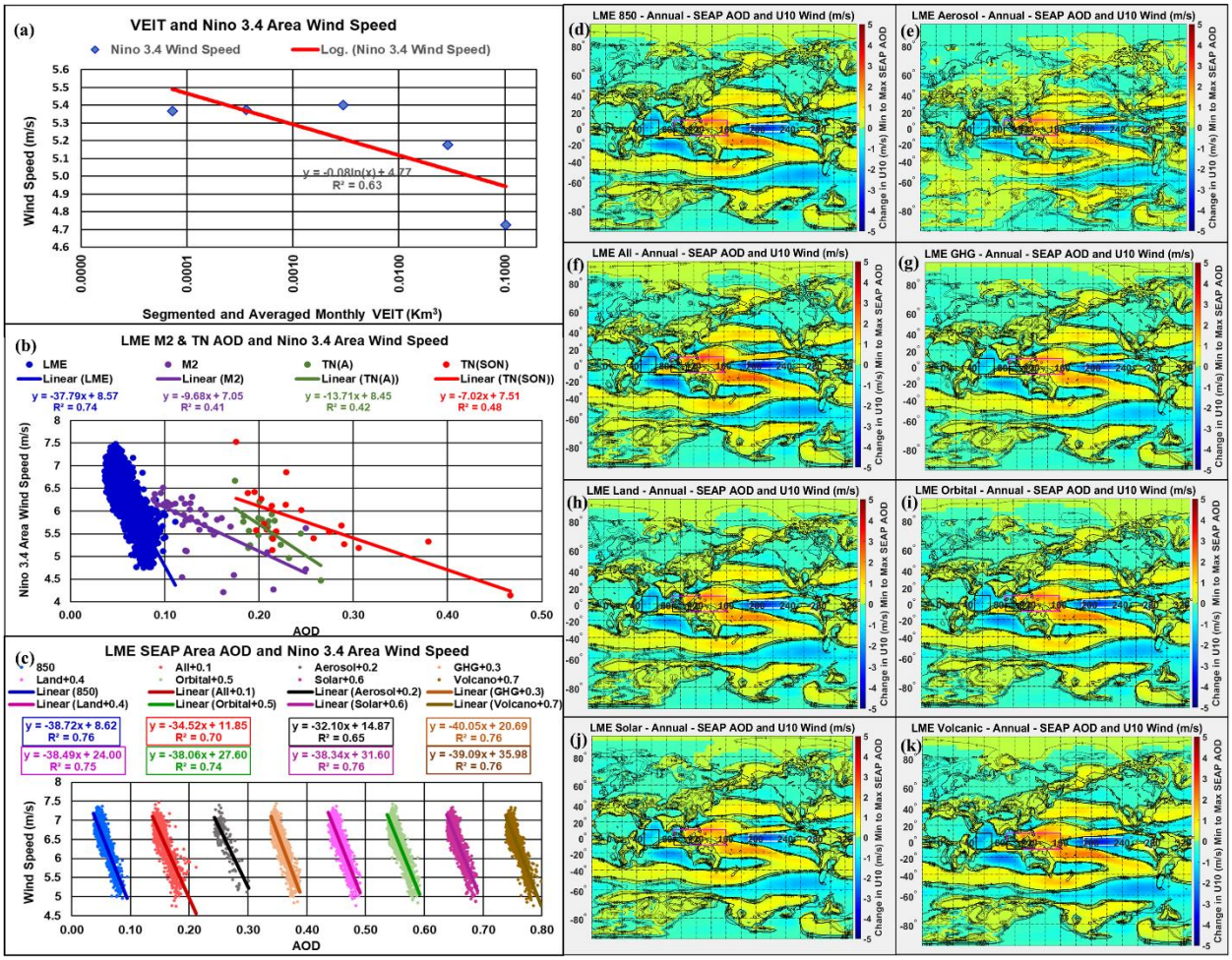

Figure. 9. Scatter plots showing: segmented annual SEAP Area VEIT and Nino 3.4 U10 wind speed (a); LME, M2 and TN annual and TN SON SEAP Area AOD and Nino 3.4 U10 (b); Scatter plots of the individual LME simulations SEAP Area AOD and Nino 3.4 U10 separated by 0.1 along the AOD axis (c); and U10 trend maps of the individual simulations named on the map titles (d) to (k)

4.6 Stage 5: Wind Speed and Nino 3.4 Area TS

Table 2 shows that increased TW speed in the Nino 3.4 area results in reduced Nino 3.4 SST. Fig. 10(a) shows that, consistent with the literature, increased Nino 3.4 area U10 velocity results in reduced Nino 3.4 TS. Fig. 10(b) shows that all the individual LME simulations show the same result with an average reduction in the Nino 3.4 TS from minimum to maximum Nino 3.4 U10 velocity of 4.51ºK consistent with the existence of an ENSO event at the minimum U10 speed. Fig. 10(b) also shows the average R^2 values across the eight individual simulations is 0.84 showing the Nino 3.4 U10 velocity controls 84% of the variation in the Nino 3.4 SST and therefore is the only agent forcing major changes in the Nino 3.4 SST and creating ENSO events.

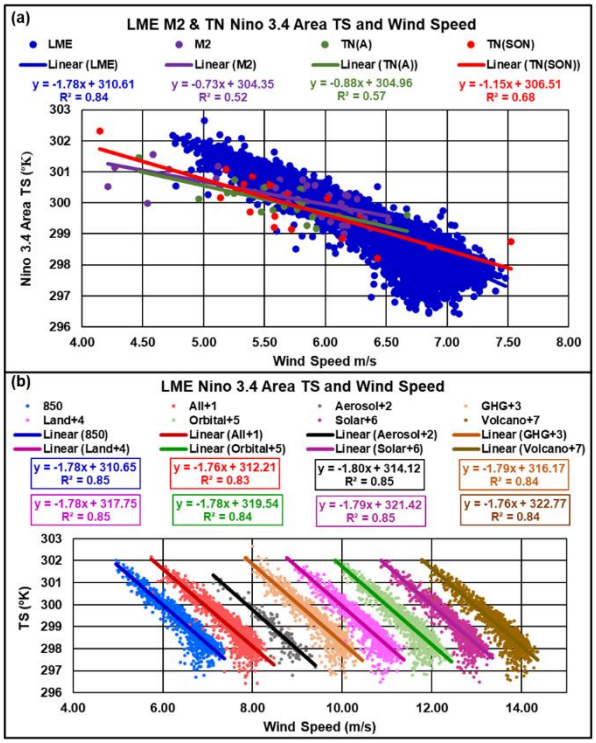

Figure 10. Scatter plots showing LME, M2 and TN annual and TN SON Nino 3.4 area TS and wind speed (a); and Scatter plots of the individual LME simulations separated by 1.0 along the wind speed axis

4.7 Niño Areas SST and the SOI

These are the prime indices used to monitor the onset and progress of an ENSO event.

4.7.1 Stage 5: Nino 3.4 SST

Table 1 shows the standard segments used for the volcano data and Table 2 and Fig. 11(a) show that increased levels of tephra result in an increased Nino 3.4 SST. Fig. 11(b) shows increasing Nino 3.4 TS with increasing SEAP AOD and Fig. 11(c) shows that all the individual LME simulations show the same result with an average increase in the Nino 3.4 TS from minimum to maximum SEAP AOD of 4.05ºK consistent with the existence of an ENSO event. Fig. 11(c) also

601 shows the average R^2 values across the eight individual simulations is 0.68 showing the SEAP
602 controls 68% of the variation in the Nino 3.4 SST and therefore is the only agent forcing major
603 changes in the Nino 3.4 SST and creating ENSO events. Fig. 7(d) to (k) show the change in TS
604 in the individual LME simulations, calculated as noted above, and show that on a global scale the
605 agent driving the TS change is the SEAP as the structure of the change is identical in each trend
606 map with only minor variations in the detail. All these figures also show within the white
607 outlined Nino 3.4 area TS rises of 3ºC to 5ºC which are consistent with the existence of an
608 ENSO event which show monthly TS rises of up to 2.53ºC during the extreme 1997 ENSO event
609 (NCEP-R1).

610

611

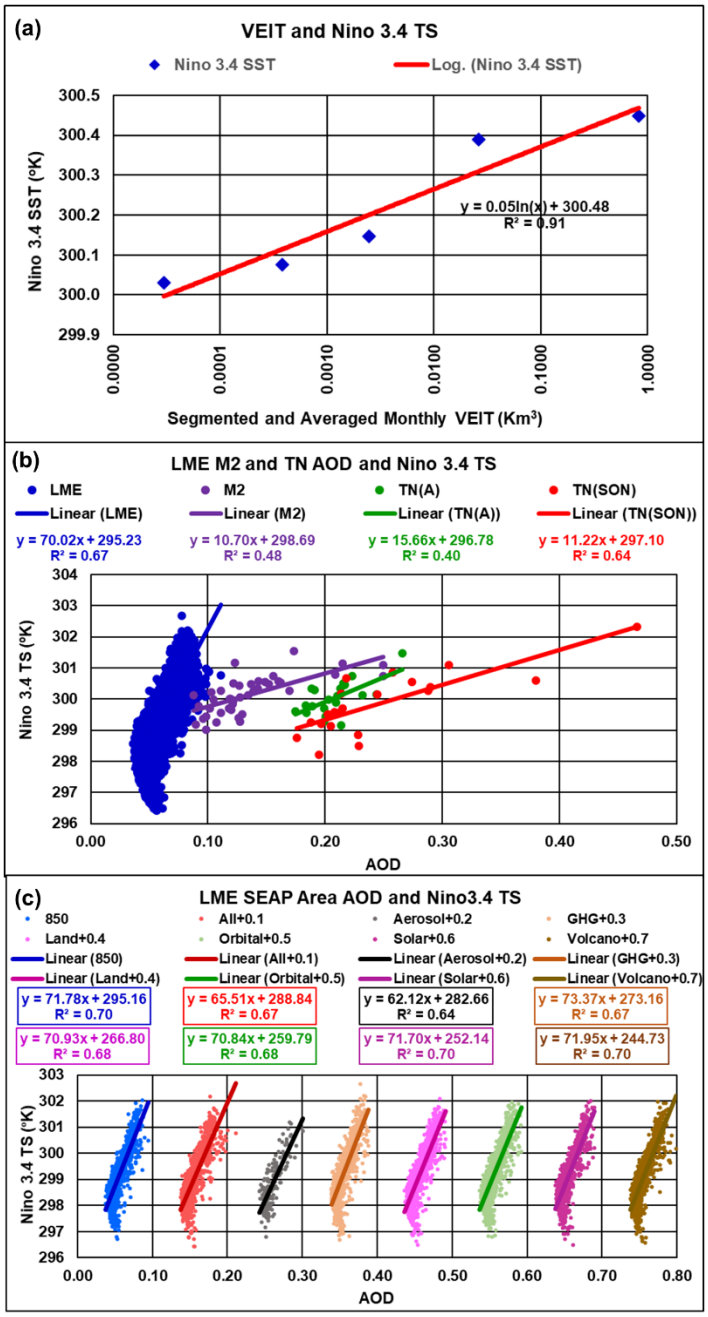

Figure 11. Scatter plots showing: segmented annual SEAP Area VEIT and Nino 3.4 TS (a); LME, M2 and TN annual and TN SON SEAP Area AOD and Nino 3.4 TS (b); Scatter plots of the individual LME simulations SEAP Area AOD and Nino 3.4 TS separated by 0.1 along the AOD axis (c)

4.7.2 Stage 5: Nino 1+2 SST

Table 1 shows the segments used for the volcano data and Table 2 and Fig. 12(a) show that increased levels of tephra result in increased Nino 1+2 SST. Fig. 12(b) shows increasing Nino 1+2 TS with increasing SEAP AOD and Fig. 12(c) shows that all the individual LME simulations show the same result with an average increase in the Nino 1+2 TS from minimum to maximum SEAP AOD of 2.78ºK consistent with the existence of an ENSO event. Fig. 12(c) also shows the average R^2 values across the eight individual simulations is 0.62 showing the SEAP controls 62% of the variation in the Nino 1+2 TS and therefore is the only agent forcing major changes in the Nino 1+2 SST and creating ENSO events. Fig. 7(d) to (k) show the change in TS in the individual LME simulations, calculated as noted above, and show that on a global scale the agent driving the TS change is the SEAP as the structure of the change is identical in each trend map with only minor variations in the detail. All these figures also show within the white outlined Nino 1+2 area temperature rises of 1.5ºC to 3ºC which are consistent with the existence of an ENSO event which show monthly TS rises of up to 4.67ºC in the 1997 ENSO event (NCEP-R1).

.

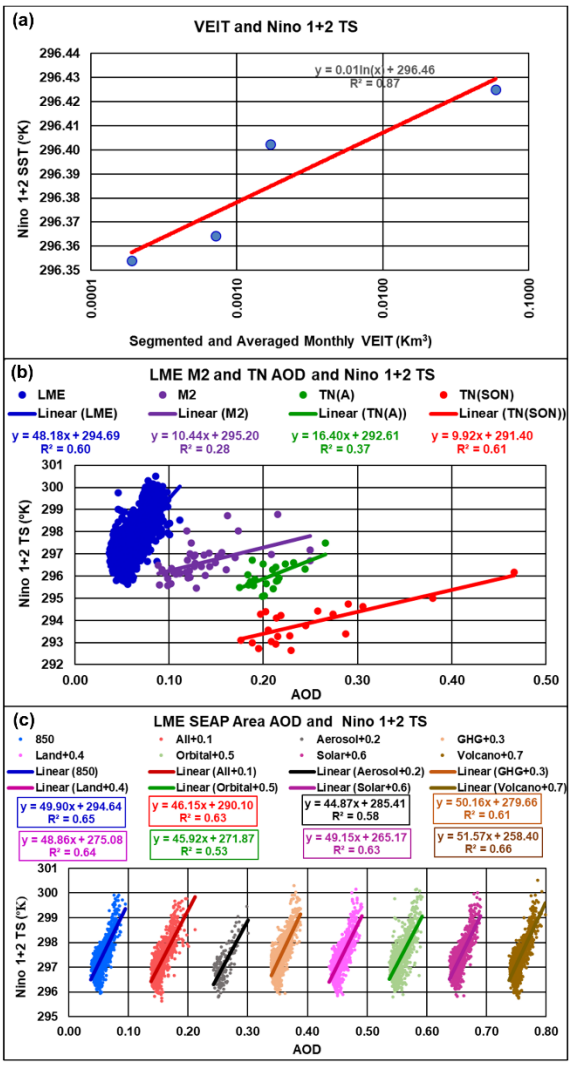

Figure 12. Scatter plots showing: segmented annual SEAP Area VEIT and Nino 1+2 SST (a); LME, M2 and TN annual and TN SON SEAP Area AOD and Nino 1+2 TS (b); and scatter plots of the individual LME simulations SEAP Area AOD and Nino 1+2 TS separated by 0.1 along the AOD axis (c)

4.7.3 Stage 6: Higher Nino 3.4 SST causes convection

Cai et al. (2015) investigating the potential changes in ENSO due to greenhouse warming note that atmospheric convection follows the highest sea surface temperature and this is confirmed here.

Table 1 shows the segments used for the volcano data and Table 2 and Fig. 13(a) show that increased levels of tephra result in reduced Nino 3.4 omega and thus increased convection. Fig. 13(b) shows the reduction in the Nino 3.4 omega with increasing SEAP AOD and Fig. 13(c) shows that all the individual LME simulations show the same result with an average reduction in the Nino 3.4 area omega from minimum to maximum SEAP AOD of 0.063 hPa/s. Fig. 13(c) also shows the average R^2 values across the eight individual simulations is 0.75 showing the SEAP controls 75% of the variation in the Nino 3.4 area omega and therefore is the only agent forcing

major changes in the Nino 3.4 area omega. Fig. 8(d) to (k) show the change in omega in the individual LME simulations, calculated as noted above, and show that on a global scale the agent driving the omega change is the SEAP as the structure of the change is identical in each map with only minor variations in the detail.

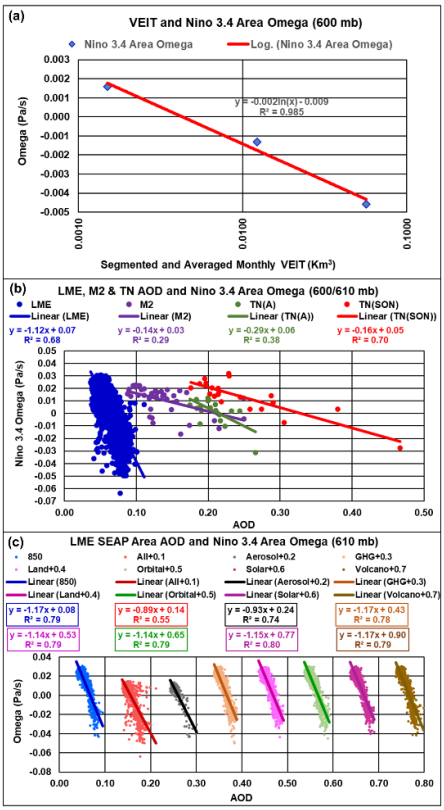

Figure 13. Scatter plots showing: segmented annual SEAP Area VEIT and Nino 3.4 area omega (a); LME, M2 and TN annual and TN SON SEAP Area AOD and Nino 3.4 Area omega (b) and scatter plots of the individual LME simulations SEAP Area AOD and Nino 3.4 area omega separated by 0.1 along the AOD axis (c).

664 ### 4.7.4 Stage 7: Southern Oscillation Index

665 Table 1 shows the standard segments used for the volcano data. The data is limited to 1876-2020
666 due to the availability of BOM SOI Data and Table 2 and Fig. 14(a) show that increased levels of
667 tephra result in a reduced SOI. Fig. 14(b) shows the reduction in the SOI with increasing SEAP
668 AOD and Fig. 14(c) shows that all the individual LME simulations show the same result with an
669 average reduction in the SOI from minimum to maximum SEAP AOD of 26.8 consistent with
670 the existence of an ENSO event. Fig. 14(c) also shows the average R^2 values across the eight
671 individual simulations is 0.63 showing the SEAP controls 63% of the variation in the SOI and
672 therefore is the only agent forcing major changes in the SOI and creating ENSO events. Fig.
673 14(d) to (k) show the change in PSL in the individual LME simulations, calculated as noted
674 above, and show that on a global scale the agent driving the PSL change is the SEAP as the
675 structure of the change is identical in each trend map with only minor variations in the detail. All
676 these figures also show within the white outlined Nino 3.4 area PSL falling by 2-3 hPa and
677 within the magenta outlined SEAP Area PSL rising by 1-3 hPa. These changes are consistent
678 with the existence of an ENSO event. In the 1997, 2006, 2015 and 2019 ENSO events the
679 NCEP-R1 data shows the annual Darwin and Tahiti PSL changed by an average of +0.81 hPa
680 and -0.32 hPa respectively.

681

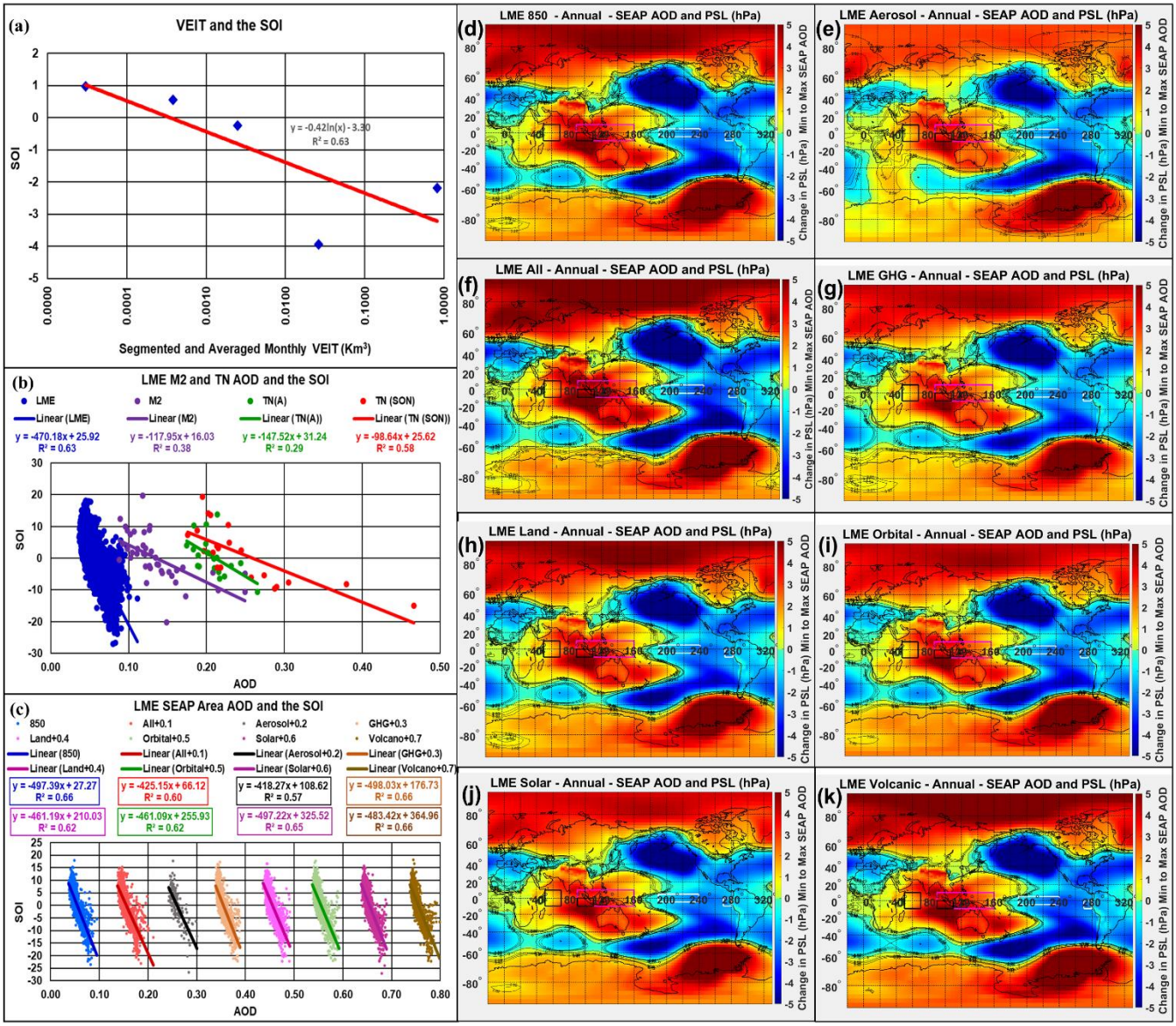

Figure 14. Scatter plots showing: segmented annual SEAP Area VEIT and the SOI (a); LME, M2 and TN annual and TN SON SEAP Area AOD and the SOI (b); scatter plots of the individual LME simulations SEAP Area AOD and the SOI separated by 0.1 along the AOD axis (c); and PSL trend maps of the individual simulations named on the map titles (d) to (k)

4.8 Other effects commonly associated with ENSO

Simultaneously with creating ENSO events the SEAP also creates Indian Ocean dipole events and drought in SEAus.

4.8.1 The Indian Ocean Dipole – May to October

Table 1 shows the standard segments used for the volcano data and Table 2 and Fig. 15(a) show that increased levels of tephra result in a positive change in the IOD. Fig. 15(b) shows increasing IOD with increasing SEAP AOD and Fig. 15(c) shows that all the individual LME simulations

show the same result with an average increase in the IOD from minimum to maximum SEAP AOD of 4.28 and the maximum IOD in the trend line in each simulation is over 2.0 which is consistent with the existence of an IOD event. Fig. 15(c) also shows the average R^2 values across the eight individual simulations is 0.73 showing the SEAP controls 73% of the variation in the IOD and therefore is the only agent forcing major changes in the IOD and creating IOD events. Fig. 7(d) to (k) show the change in TS in the individual LME simulations, calculated as noted above, and show that on a global scale the agent driving the TS change is the SEAP as the structure of the change is identical in each trend map with only minor variations in the detail. It is also worth noting that the SEAP covers the eastern area used to calculate the IOD and therefore has a direct and immediate impact on one element of the IOD calculation whilst the warming of the eastern IOD area is caused by the reduced wind speed which can be seen resulting from the increased SEAP AOD in Fig. 9 (d) to (k).

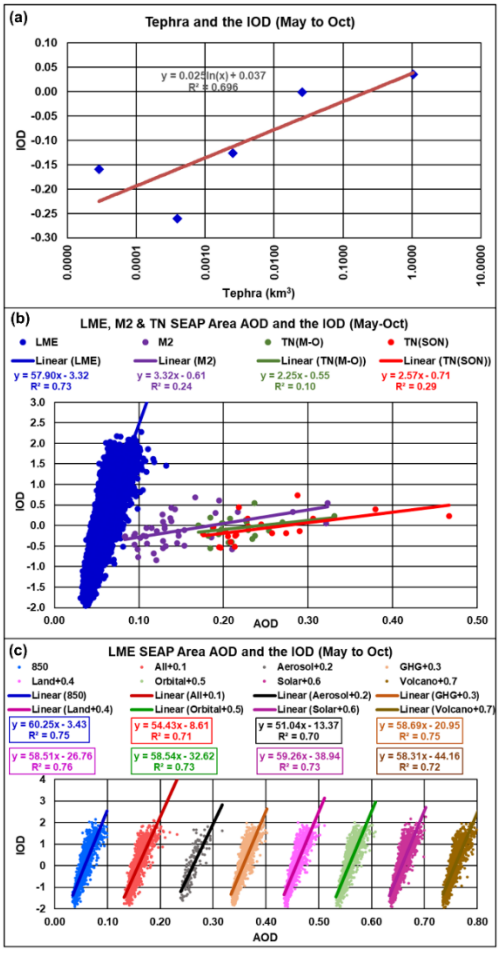

Figure 15. Scatter plots showing: segmented annual SEAP Area VEIT and the IOD (a); LME, M2 and TN annual and TN SON SEAP Area AOD and the IOD (b); and scatter plots of the individual LME simulations SEAP Area AOD and the IOD separated by 0.1 along the AOD axis (c).

4.8.2 Pressure south eastern Australia (April to October)

As well as perturbing the Walker Circulation by reducing convection in the SEAP Area, the SEAP simultaneously moves convection in the southern regional Hadley circulation south which moves the regional sub-tropical high south creating anomalous high pressure over SEAus.

Table 1 shows the segments used for the volcano data for the period 1903-2020 which is limited by the availability of BOM data. Pressure data is from the BOM station 86071 at 9:00 am 1903 to 2008 and NCEP-R1 2009 to 2020 for 144º to 146º E and 37º to 38º S. The two data sets correlate well between 1948 and 2008 at 0.96. and Table 2 and Fig. 16(a) show that increased levels of tephra result in increased SEAus PSL. Fig. 16(b) shows increasing SEAus PSL with increasing SEAP AOD and Fig. 16(c) shows that all the individual LME simulations show the same result with an average increase in the SEAus PSL from minimum to maximum SEAP AOD of 3.7 hPa. Fig. 16(c) also shows the average R^2 values across the eight individual simulations is 0.46 showing the SEAP controls 46% of the variation in the SEAus PSL and therefore is an agent forcing major changes in the SEAus PSL. Fig. 14(d) to (k) show the change in PSL in the individual LME simulations, calculated as noted above, and show that the agent driving the PSL change is the SEAP as the structure of the change is identical in each trend map with only minor variations in the detail. These Figures show a band of high pressure originating in the western SEAP Area and extending across the Australian continent with increased pressure over the Great Australian Bight (GAB) which will force cold fronts crossing the Indian Ocean to the GAB to the south thereby reducing rainfall in SEAus. It is worth noting that: the All forcings LME simulation shows significantly higher pressure across the GAB and all of southern Australia in Fig.14(f) compared to all other LME forcings in Fig. 14; and the GHG simulation shows no significant difference to the other individual simulations.

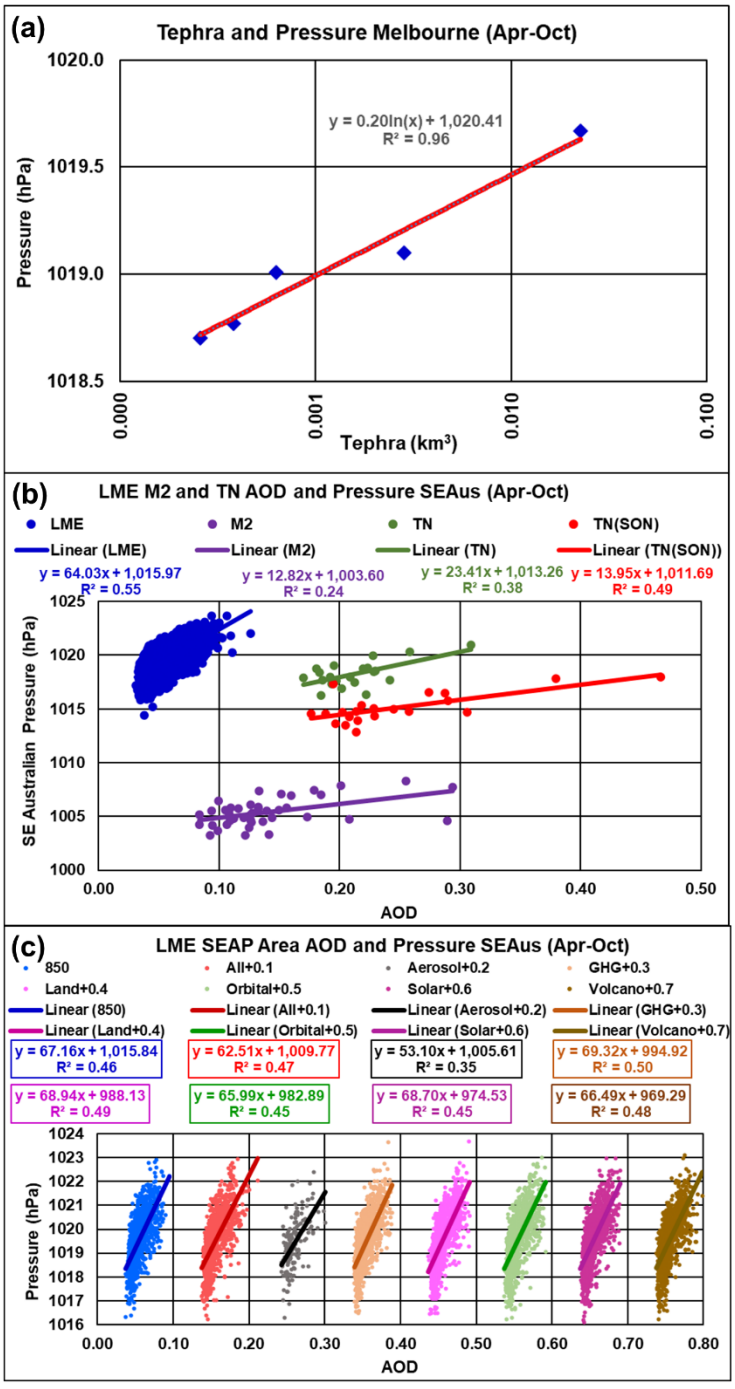

Figure 16. Scatter plots showing: segmented annual SEAP Area VEIT and pressure in Melbourne (a); LME, M2 and TN annual and TN SON SEAP Area AOD and pressure in SEAus (b); scatter plots of the individual LME simulations SEAP Area AOD and pressure separated by 0.1 along the AOD axis (c)

4.8.3 Rainfall south eastern Australia (April to October)

Table 1 shows the segments used for the volcano data. Rainfall data is from the BOM Melbourne station 86071 (1870-2014) and station 86039 (2015-2020). Average rainfall for the month was

744 inserted into the three months without data. Table 2 and Fig. 17(a) show that increased levels of
745 tephra result in reduced SEAus rainfall. Fig. 17(b) shows reducing SEAus rainfall with
746 increasing SEAP AOD and Fig. 17(c) shows that all the individual LME simulations show the
747 same result with an average reduction in the SEAus rainfall from minimum to maximum SEAP
748 AOD of 183 mm. Fig. 17(c) also shows the average R^2 values across the eight individual
749 simulations is 0.39 showing the SEAP controls 39% of the variation in the SEAus rainfall and
750 therefore is an agent forcing significant changes in the SEAus rainfall. Fig. 17(d) to (k) show the
751 change in SEAus rainfall in the individual LME simulations, calculated as noted above, and
752 show that on a global scale the agent driving the PRECL change is the SEAP as the structure of
753 the change is identical in each trend map with only minor variations in the detail. These Figures
754 also show a band of reduced rainfall originating in the western SEAP Area and extending across
755 the Australian continent and the Pacific Ocean as far as the southern tip of South America. In
756 SEAus the reduction is 1.0 mm/day and it is worth noting that: the All forcings LME simulation
757 shows significantly lower rainfall in south eastern Australia in Fig.17(f) compared to all other
758 LME forcings in Fig. 17; and the GHG simulation shows no significant difference to the other
759 individual simulations.

760

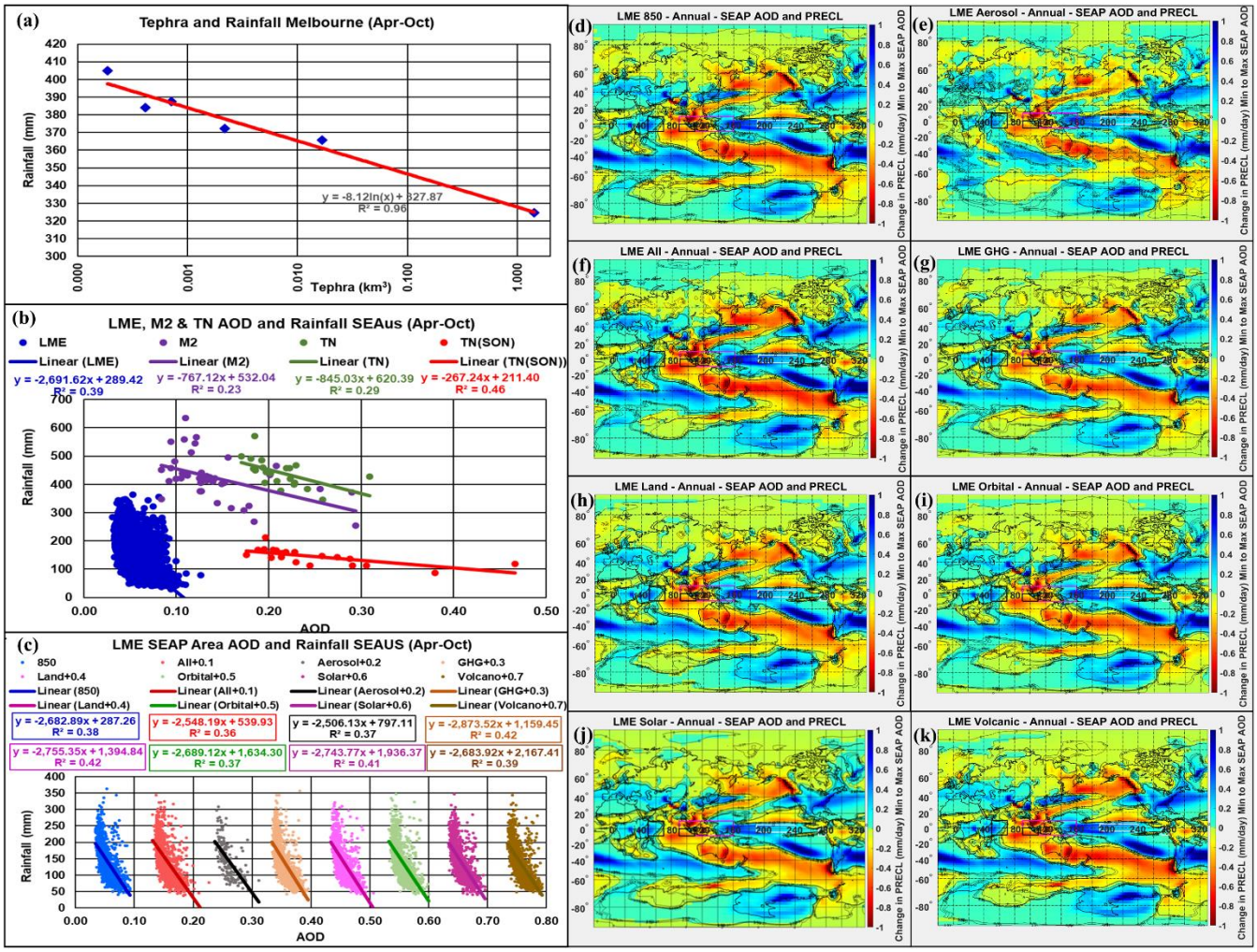

761

762 **Figure 17**. Scatter plots showing: segmented April to October SEAP Area VEIT and rainfall in
763 Melbourne (a); LME, M2 and TN April to October and TN SON SEAP Area AOD and rainfall
764 in SEAus (b); scatter plots of the individual LME simulations SEAP Area AOD and rainfall
765 separated by 0.1 along the AOD axis (c); and annual rainfall trend maps from the individual
766 simulations named on the map titles (d) to (k)

767 ### 4.8.4 Global Temperature

768 Table 1 shows the segments used for the volcano data and Table 2 and Fig. 18(a) show that
769 increased levels of tephra result in an increased global TS. Fig. 18(b) shows increasing global TS
770 with increasing SEAP AOD and Fig. 18(c) shows that all the individual LME simulations show
771 the same result with an average increase in the global TS from minimum to maximum SEAP
772 AOD of 0.65ºK which is consistent with the existence of an ENSO event. Fig. 18(c) also shows
773 the average R^2 values across the eight individual simulations is 0.34 showing the SEAP controls
774 34% of the variation in the global TS and therefore is an agent forcing a significant change in the
775 global TS. Fig. 7(d) to (k) show the change in TS in the individual LME simulations, calculated
776 as noted above, and show that on a global scale the agent driving the TS change is the SEAP as
777 the structure of the change is identical in each trend map with only minor variations in the detail.
778 These Figures show higher temperatures extending to both poles and some areas of the Arctic,
779 Alaska, and the Antarctic, the Bellingshausen, Amundsen and Ross seas, showing temperature
780 rises of over 4º K. It is suggested that this global temperature rise is created by the reduction of
781 convection in the SEAP Area one of, if not the greatest, area of convection in the World which
782 reduces the heat flow away from the surface of the Earth and also reduces the wind speed which
783 forces the temperature rise.

784 **Note**: the TN(A) and TN(SON) temperature data is delayed by one year in this analysis as
785 comparing the same years shows no statistically significant connection but the 1 year lagged data
786 does, possibly due to the high levels of biomass burning late in the year in some years in recent
787 decades forcing an extreme ENSO event which affects the following year more than the current
788 year because of the timing.

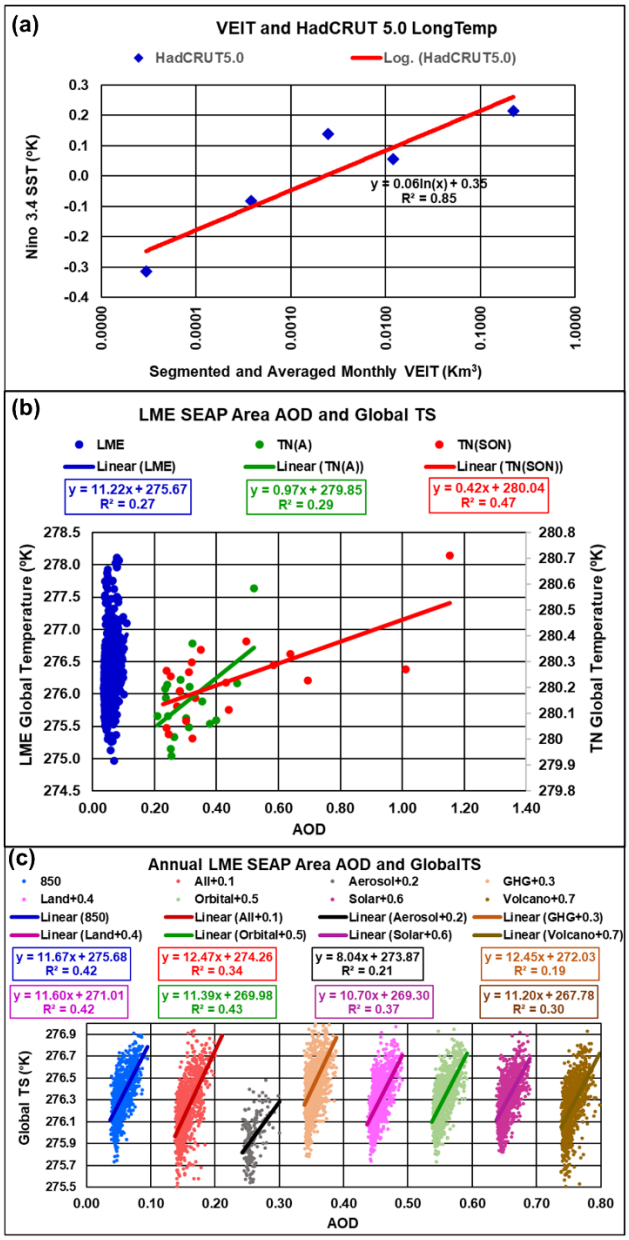

Figure 18. Scatter plots showing: segmented annual SEAP Area VEIT and global temperature (a); LME and TN annual and TN SON SEAP Area AOD and global temperature (b); scatter plots of the individual LME simulations SEAP Area AOD and global temperature separated by 0.1 along the AOD axis (c);

796

A	Surface Temp SEAP Area	GVP	LME	MERRA-2	TN (SON)
1	R	-0.81	**-0.59**	*-0.39*	**-0.68**
2	R^2	0.66	**0.35**	*0.15*	**0.46**
3	Trend/unit AOD (º K)		-12.63	-1.56	-2.10
4	Change AOD/tephra range (º K)	-0.33	-1.06	-0.25	-0.61
B	**Omega SEAP Area**				
1	R	0.78	**0.82**	**0.61**	**0.82**
2	R^2	0.61	**0.68**	**0.37**	**0.68**
3	Trend/unit AOD (Pa/s)		0.48	0.10	0.10
4	Change AOD/tephra range Pa/s	0.008	0.035	0.02	0.03
C	**Wind Speed Nino 3.4 Area**				
1	R	-0.79	**-0.86**	**-0.64**	**-0.69**
2	R^2	0.63	**0.74**	**0.41**	**0.48**
3	Trend/unit AOD (m/s)		**-37.8**	**-9.68**	**-7.02**
4	Change over AOD range (m/s)	-0.55	**-2.76**	**-1.56**	**-2.04**
D	**Wind Speed and TS Nino 3.4 Area**				
1	R		**-0.92**	**-0.72**	**-0.82**
2	R^2		**0.84**	**0.52**	**0.68**
3	TS/unit TW speed change		**-1.78**	**-0.73**	**-1.15**
4	Change over AOD range		**-4.88**	**-1.69**	**-3.88**
E	**Nino 3.4 SST**				
1	R	0.95	**0.82**	**0.69**	**0.81**
2	R^2	0.91	**0.67**	**0.48**	**0.64**
3	Trend/unit AOD (º K)		**70.02**	**10.70**	**11.22**
4	Change over AOD range (º K)	0.47	**5.11**	**1.72**	**3.27**
F	**Nino 1+2 SST**				
1	R	0.93	**0.77**	**0.53**	**0.78**
2	R^2	0.87	**0.60**	**0.28**	**0.61**
3	Trend/unit AOD (º K)		**48.18**	**10.4**	**9.92**
4	Change over AOD range (º K)	0.07	**3.52**	**1.68**	**2.89**
G	**SOI**				
1	R	-0.79	**-0.79**	**-0.62**	**-0.76**
2	R^2	0.63	**0.63**	**0.38**	**0.58**
3	Trend/unit AOD		**-470**	**-118**	**-99**
4	Change over AOD range	-4.29	**-34.32**	**-18.99**	**-28.70**

797

H	**Convection Nino 3.4 Area**				
1	R	-0.99	**-0.82**	**-0.54**	**-0.84**
2	R^2	0.99	**0.68**	**0.29**	**0.70**
3	Trend/unit AOD		**-1.12**	**-0.14**	**-0.16**
4	Change over AOD range	-0.006	**-0.08**	**-0.02**	**-0.05**
I	**IOD (May to October)**				
1	R	0.84	**0.85**	**0.49**	*0.54*
2	R^2	0.70	**0.73**	**0.24**	*0.29*
3	Trend/unit AOD		**57.9**	**3.32**	**2.57**
4	Change over AOD range	0.26	**5.85**	**0.80**	**0.75**
J	**Pressure SE Australia (Apr-Oct)**				
1	R	0.98	**0.74**	**0.49**	**0.70**
2	R^2	0.96	**0.55**	**0.24**	**0.49**
3	Trend/unit AOD		**64.03**	**12.82**	**13.95**
4	Change over AOD range	0.91	**5.63**	**2.59**	**4.06**
K	**Rainfall SE Australia (Apr-Oct)**				
1	R	-0.98	**-0.62**	**-0.48**	**-0.68**
2	R^2	0.96	**0.39**	**0.23**	**0.46**
3	Change over AOD range	-73	**-256**	**-162**	**-78**
4	% age fall over AOD range	-18%	**-100%**	**-35%**	**-47%**
L	**Global Temperature Annual**	**GVP**	**LME**	**TN(A)***	**TN(SON)***
	R	0.92	**0.52**	**0.54**	**0.69**
	R^2	0.85	**0.27**	**0.29**	**0.47**
	Trend/unit AOD		**11.22**	**0.97**	**0.42**
	Change over AOD range	0.53	**0.84**	**0.30**	**0.39**

Table 2. Correlations and changes from: minimum to maximum tephra/AOD and trend/unit AOD; for the parameters shown in the GVP, LME, M2 and TN datasets. Correlations are all at significance <0.01 (bold) except: M2 SEAP Area TS; TN (SON) IOD; and TN(A) global temperature which show significance <0.02 (italic). * One year lag.

5 DISCUSSION

The results show: increasing levels of tephra and AOD in the SEAP Area result in the same change in the parameters analysed; and statistically significant correlations in all cases which establishes the link between tephra/aerosols and ENSO and the associated events. It is clearly understood that correlation between events A and B does not prove causation from A to B or vice versa. Thus, the causal relationship between the SEAP and the ENSO must be demonstrated in other ways.

5.1 ENSO

The similarity of the power spectra of the Nino 3.4 SST and the SEAP Area tephra (Fig. 3); and the clear correlations between volcanic tephra in the SEAP Area, ENSO and the other associated events demonstrated in this paper show a close relationship exists. **Crucially, volcanic eruptions are caused by deep earth tectonic processes and cannot be caused by ENSO or other surface events. Therefore, the causal direction must run from the volcanic eruptions to ENSO and the associated events including the global temperature.**

All the data shows that the effects of volcanic tephra and anthropogenic aerosols on ENSO, and other events are immediate with a simple physical explanation and Table 2 and Fig. 7 show that the LME Nino 3.4 SST rises by 5.11°C from 297.89°C to 303.00°C and the SOI falls from +8.05 to -26.27 accurately reflecting the range of these indices from La Nina to El Nino events without using correlation. Also, the TN (SON) data shows a much greater variation than the TN(A) data reflecting the much greater variation in the measured AOD and explaining the ASON anomaly in Fig. 4.

The LME data used in this paper is forced by eight agents and, in this modelling, there is no mechanism to create aerosols in south east Asia during an ENSO event and hence the causal direction must run from the aerosols to the ENSO events. In addition, the aerosol forcings in all LME runs are fixed at 1850 values except for the “ozone and aerosol” and “all” runs and there can therefore be no forcing of the aerosols by any agent within these six runs and the causal direction must flow from the aerosols to the ENSO events.

The M2 reanalysis assimilates measured aerosol data and as Appendices A and B show the aerosol sources are volcanoes, gas flares and fires lit by the local population, the causal direction must be from the aerosols to the ENSO events as source of the aerosols is known and they are assimilated and not generated within the model by ENSO.

Fig. 4 clearly shows that the character of ENSO as measured by the Nino 3.4 SST has changed since 1980 when the extreme anthropogenic SEAP started to appear and with the high correlations of the anthropogenic SEAP in SON with ENSO it is clear that the change is driven by the SEAP and since Appendix B shows that the SON anthropogenic SEAP is caused by fires deliberately lit to clear land and agricultural waste the causal direction must run from the SEAP to ENSO.

ENSO is highly seasonal and this paper provides an explanation for the seasonality. Rainfall in the CSEAP area and the Nino 3.4 SST correlate at -0.57 significance <0.15 with the SST reducing when rainfall in the SEAP Area is high. This clearly supports the hypothesis that the SEAP is the major cause of ENSO events as the south east Asian monsoon rainfall washes the aerosols out of the atmosphere enabling convection to be re-established in the region to drive the

TWs which force the Pacific warm pool back to the western Pacific Ocean which ends the ENSO event.

Eight LME modelling runs and the M2 reanalysis exhibit very low or negative correlations between the SEAP AODVIS in the individual runs as shown in the correlation matrix in Appendix E with an overall average 0.0008. Hence the datasets are independent. All these eight LME and M2 datasets show correlations with the ENSO indices at significance of <0.01 or less and the chance that all these eight independent datasets show the same result and are wrong is the product of the significances i.e., 0.01^8 or 10^{-16}, a vanishingly small number.

Finally, two competing ENSO theories exist and this paper, which is a specific case of the steady state with high frequency forcing theory, confirms this theory by clearly showing that the "high frequency" forcing is and has always been caused by SEAP Area volcanic eruptions and therefore shows the "oscillator" theories to be invalid.

5.2 Rainfall and pressure south eastern Australia

Reduced rainfall and increased pressure in SEAus cannot create aerosols in the SEAP Area. I show that drought in SEAus which has commonly been attributed to ENSO and/or IOD events is created simultaneously by the SEAP which further confirms the causal relationship flows from the SEAP to ENSO and the associated events.

5.3 Global temperature

Table 2 and Fig. 18 show global temperature rises which reflect measured temperature rises during ENSO events.

5.4 Causal direction

Therefore with:

1. Volcanic aerosols demonstrating conclusively that SEAP Area aerosols must be the cause of ENSO events;
2. The LME, M2 and TN data showing a clear connection between the SEAP and ENSO indices which mirrors reality without correlation;
3. The individual LME, M2 and TN time series analyses showing the same results with a vanishingly small chance of error;
4. The IOD showing a clear connection to the SEAP;
5. Higher pressure and drought in SEAus showing a clear connection the SEAP; and
6. Higher global temperatures resulting from increased SEAP AOD and tephra;

The inevitable conclusion is that the SEAP is the driver of ENSO and these associated events.

5.5 SEAP Area Aerosol Optical Depth

It is clear from all the graphs that the SEAP Area AOD levels in the LME and M2 are far too low with annual averages of 0.055 (26%) and 0.147 (71%) respectively compared to the Terra

880 average of 0.208 (annual) and 0.247 (SON). Additionally no LME data falls within the Terra
881 range with the highest LME AOD being 37% lower than the lowest Terra data and whilst 9.8%
882 of the M2 data falls within the Terra range at least 51% should fall within this range as M2 is
883 stated to assimilate aerosol data and the years 2000 to 2020 are common to both datasets.

884 My analysis of twenty three CMIP6 models also shows SEAP Area AOD levels which are far
885 too low. This paper will be submitted for review in the next few weeks and will be referenced
886 here.

887 Obviously these discrepancies require further analysis.

888 ## 6 FUTURE RESEARCH

889 To finally confirm these conclusions, a further LME style analyses should be undertaken in
890 which:

891 1. An aerosol plume is created in the model which ramps up from the naturally low level in
892 February to reach the same AOD as the extreme SEAP of October 2006 in March,
893 continues at the same level to October and ramps down in November to the naturally low
894 level in December. This plume to be applied in the model with random returns from 2 to
895 10 years to mimic the actual return frequency of ENSO; and

896 2. Repeating 1 with reducing levels of AOD from February to October to determine the
897 minimum AOD level over SE Asia which is required to cause an ENSO event.

898 This analysis will conclusively demonstrate that ENSO events are caused by the SEAP and
899 determine the AOD levels required to do so.

900 ## 7 CONCLUSIONS

901 The GVP volcanic eruption data (151 years), LME (1.156 years), M2 (41 years) and TN (20
902 years) all confirm the direct connection between the SEAP and ENSO in multiple independent
903 ways.

904 Causal analysis showing that the relationship must flow from the SEAP to ENSO.

905 I therefore conclude that the SEAP is unique and is the sole trigger and sustaining agent for
906 ENSO events.

907 This paper brings five important elements into climate change analysis:

908 **First**: **All Volcanic tephra** from all eruptions and not just sulphate aerosols from large eruptions
909 must be included in climate modelling as they are the prime cause of ENSO events and are
910 therefore the primary interannual climate forcing agent;

911 **Second**: **Aerosol Regional Dimming**, the surface radiative forcing caused by the annual
912 apparitions of the eight major continental scale, aerosol plumes identified in this paper which
913 now occur each year, the anthropogenic elements of which did not exist before the middle of the
914 20^{th} century, must be incorporated in climate models at temporal and geographic resolutions
915 which will adequately model their effects. Global, seasonal, annual and decadal averages are
916 insufficient as the climate forcing effects of the plumes only exist when the plume exists and the
917 averaging process reduces the intensity of the plumes and destroys their seasonal effects which,

as this paper shows, include the intensification of ENSO events and the perturbation of the major atmospheric circulation systems, the Hadley and Walker Cells.

Note: The residence time of aerosols in the troposphere is short – the IPCC AR5 (Stocker et al., 2013) suggested a period of 1 to 3 weeks for volcanic aerosols.

Third: **ENSO** Since the SEAP causes ENSO events it follows that this aerosol plume causes an increase in the global temperature, most likely through the modification of the large-scale atmospheric circulation systems (especially convection in SE Asia) instead of just cooling the region under the plume through direct surface forcing as is commonly assumed. It is also likely that the increases in the AOD of the SEAP since 1980 in non-extreme years such as 1999 and 2001 will also have affected the global temperature. This requires further investigation.

Fourth: **Multiple Plumes**: The effects of combinations of the eight anthropogenic, continental scale aerosol plumes require investigation as the combined effects of such plumes may be radically different from the effects of individual plumes and this may, for example, provide an explanation for the ridiculously resilient ridge of high pressure in the north east Pacific Ocean which has affected rainfall in western north America in recent years.

Finally I concur with Booth et al. (2012) that emissions of carbonaceous aerosols are directly addressable by government policy actions and suggest that this is an urgent necessity to mitigate future severe anthropogenic ENSO events in the Austral spring which Timbal and Drosdowsky (2013) link to drought in Australia.

Fifth SEAP Area Aerosol Levels: The reasons for models incorporating aerosol levels which are too low must be investigated and the levels corrected.

8 APPENDIX A: THE VOLCANIC SOUTH EAST ASIAN AEROSOL PLUME

This paper analyses the volcanic South East Asian aerosol Plume (SEAP) which is created by volcanoes within the region 90º to 160º E 10º S to 10º N (SEAP Area). Fig. 1 shows this region which includes nearly all Indonesia, Malaysia, Brunei, Papua New Guinea and parts of the Philippines and Thailand and the Global Volcanism Program (GVP) overlay of volcano locations, each red triangle is either one or, at this scale, a cluster of volcanoes.

The GVP database of volcanic eruptions (Venzke, 2013) shows that the SEAP Area hosted over 26% of all the global volcanic eruptions from 1800 to 2020 whilst covering only 3% of the Earth's surface. Simkin and Siebert (2000) reported that 16 volcanoes have been erupting nearly continuously for 30 years and that 5 of these volcanoes are in the SEAP Area. Hence the SEAP Area hosts an unusually high percentage of the global volcanic activity and within it Indonesia is "the most volcanically active nation on Earth" (USGS) https://www.usgs.gov/center-news/revolutionizing-volcano-monitoring-indonesia .

It is also worth noting that the median duration of a volcanic eruption is 7 weeks (Simkin & Siebert, 2000). The Intergovernmental Panel on Climate Change (IPCC) Assessment Report 5 (AR5) in Fig. 1 of section FAQ 11.2 notes that the effect of volcanic eruptions on the lower atmosphere (and therefore the surface) is "cooling because the reduction of sunlight overwhelms any increased downward energy emitted by the volcanic cloud" and also states the residence time in the troposphere of "1 to 3 weeks" for volcanic ash. Hence a volcanic ash plume will have a median residence time of 8 to 10 weeks in the atmosphere – 7 weeks of eruption followed by 1 to

3 weeks of residence and crucially, during this time, because the source is at a fixed location, the plume and its effects are stationary on the Earth's surface.

The volume of tephra ejected by volcanoes in the SEAP Area was calculated as shown in Appendix D.

The VEIT data was summed for each decade from 1870 to the present and when restricted to April to October (the wet season in South Eastern Australia (SEAus)) Fig. A1 shows the 2000 to 2009 VEIT level was 2.89 times the 20th century average. This is a period which closely matches the SEAus Millennium Drought, 1998 to 2008, the cause of which has not yet been determined.

Spread of tropospheric volcanic tephra: Fig. A2 shows an image of the eruption of the Sangeang Volcano in Indonesia which continued for 1.5 years from May 2014 to November 2015 (GVP database) at an estimated VEI of 3 (GVP) suggesting the majority of the tephra remained in the troposphere. This image demonstrates how quickly the aerosol plume spreads from a point source to about 250 km width in the lower right of the image after travelling about 400 Km. Noting that Indonesia, which covers a significant part of the SEAP Area, is "the most volcanically active nation on Earth" (USGS) it is easy to see how volcanic tephra from multiple simultaneous eruptions can significantly affect the AOD and the surface solar radiation in the SEAP Area.

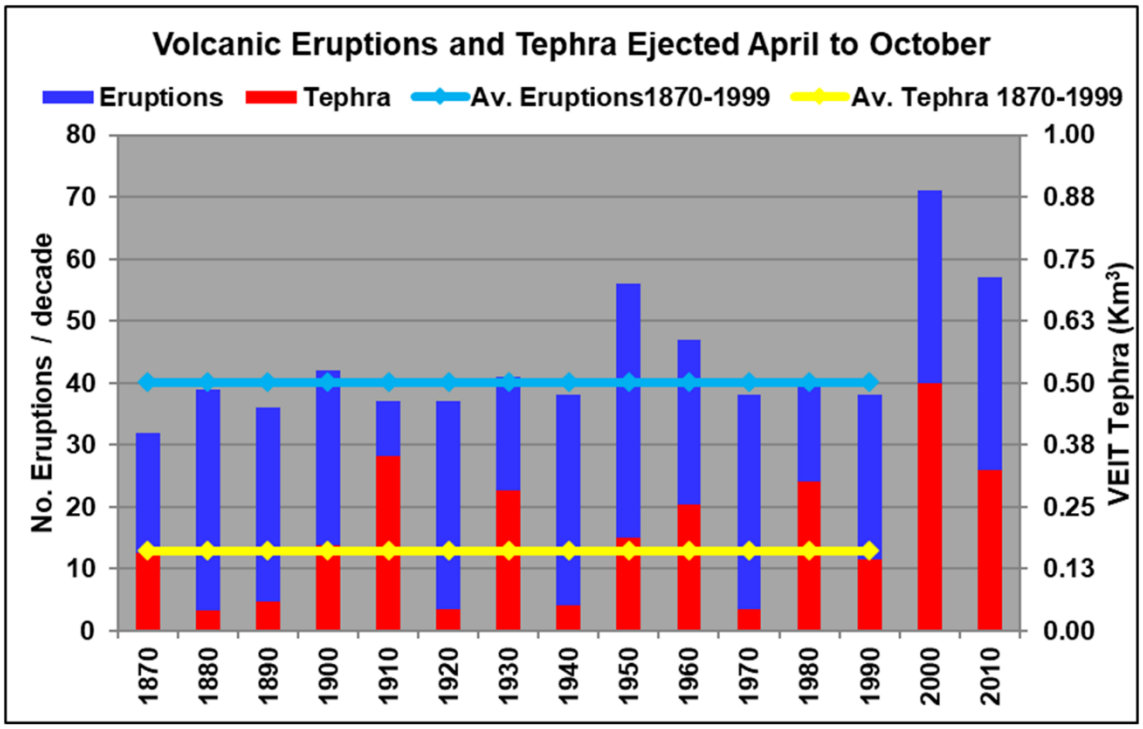

Figure A1. Decadal total and average volcanic eruptions and tephra volume in the SEAP Area from April to October. Averages from 1870 to 1999. Source GVP database. **Note**: The 1883 Krakatau eruption which ejected an estimated 10 to 100 Km^3 of tephra is not included as it would dominate the graph.

984

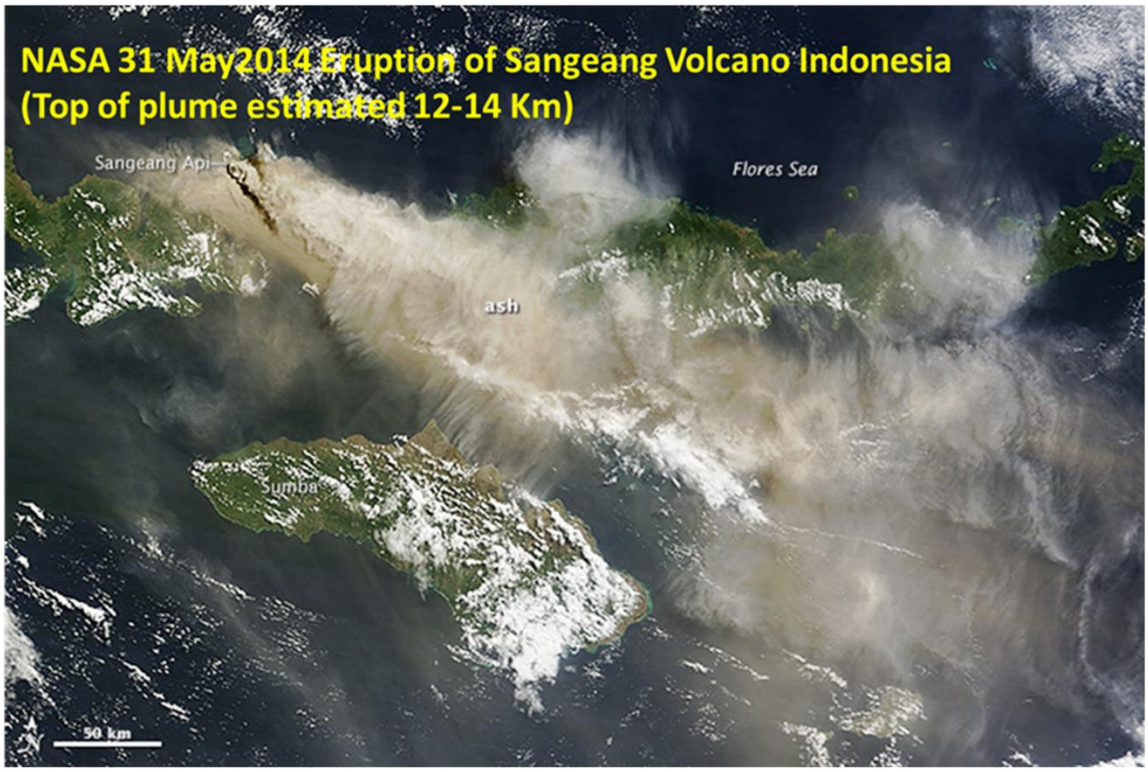

985

986 **Figure A2**. Aerosol plume emanating from Sangeang Volcano May 2014. Source NASA.

987

8.1 Tectonic activity SEAP Area

The increased level of volcanic/tectonic activity in the SEAP Area in recent decades is confirmed by the increase in the number of earthquakes. Earthquake activity increased from the early 1980's to 2005, declined to 2009 and has since increased again. The USGS provides earthquake data from 1973 at: https://www.usgs.gov/natural-hazards/earthquake-hazards/science/20-largest-earthquakes-world?qt-science_center_objects=0#qt-science_center_objects and Fig. A3 shows that the average number of earthquakes per month in the SEAP Area was 71 between 1973 and 1982. The red line marks this average plus 3 standard deviations calculated from the same period and shows that from 1995 to 2009 and 2013 to 2020 there was a significant (> 3 std deviations) increase in the number of earthquakes which peaked at 1,303 in January 2005 after the Boxing Day earthquake and tsunami. In May 2009 the number of earthquakes fell below the red line for the first time since January 1995 for a short time but in 2013 increased again and continued at this level until 2020.

The spate of major earthquakes, magnitude greater than 8.0, from 1985 to 2013 seen in Fig. A3 also confirms the exceptional increase in tectonic activity in this period.

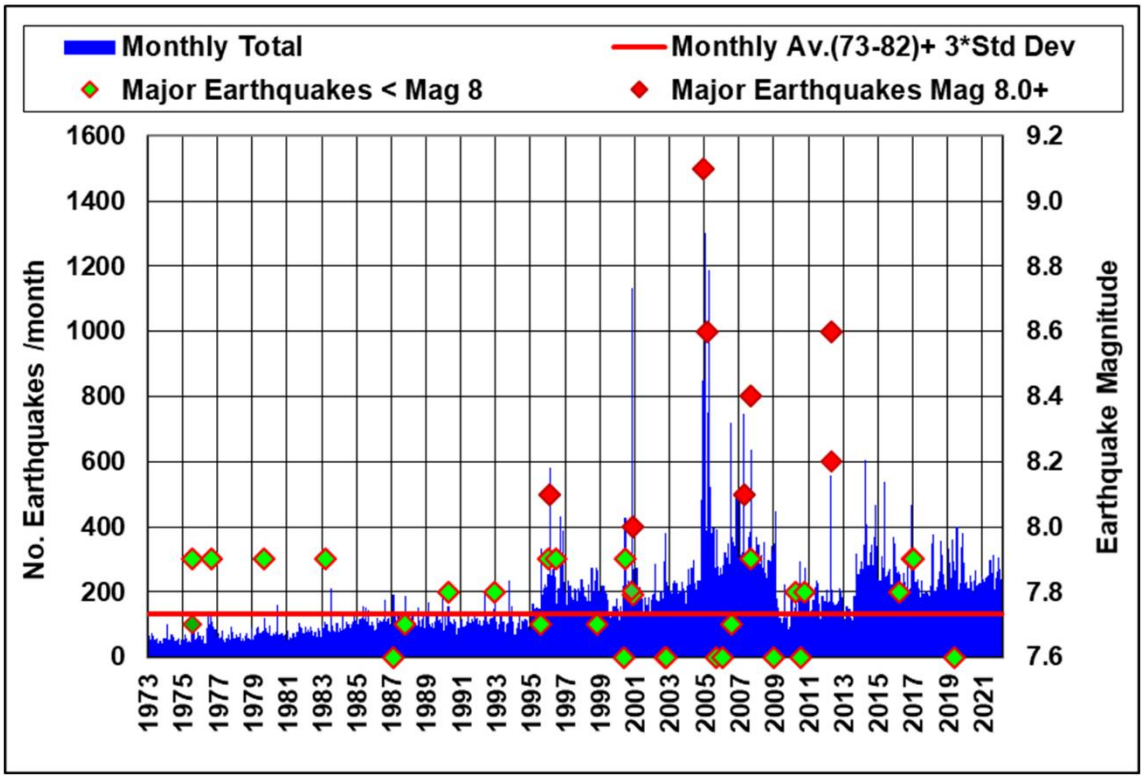

Figure A3. Total monthly earthquakes 1973 – 2021 SEAP Area with major events magnitude 7.6+ shown. Source: USGS earthquake database.

9 APPENDIX B: THE ANTHROPOGENIC SOUTH EAST ASIAN PLUME

The anthropogenic SEAP is one of eight continental scale plumes, Fig. B1, B2 and B3, and the AOD of the SEAP is shown in Fig. B4 where it is clear that SON is the season when the AOD is at its maximum. Table B1 shows the aerosol sources of the eight plumes.

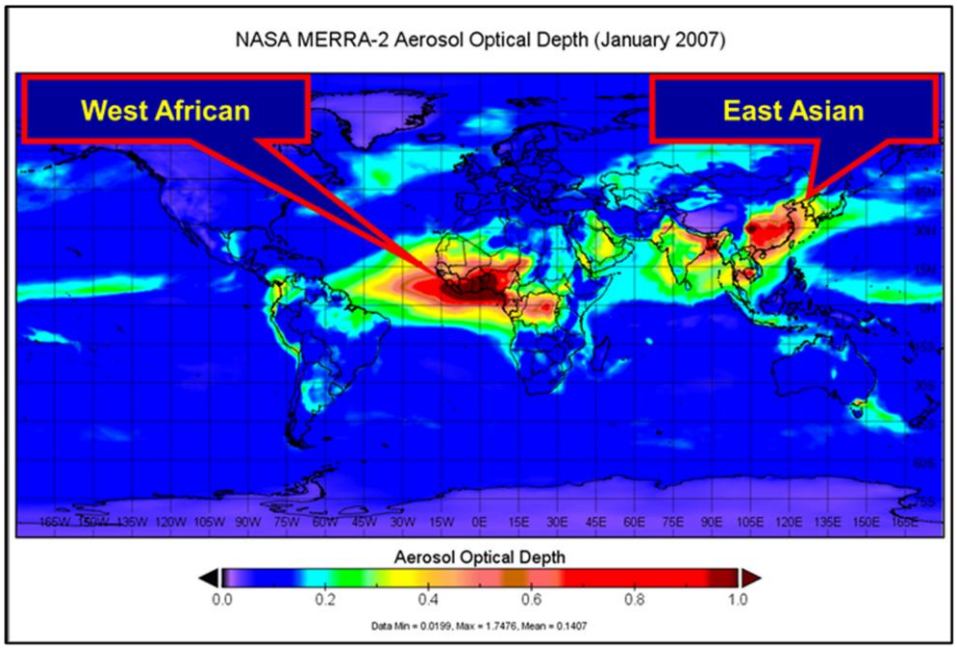

Figure B1. MERRA-2 AOD Jan 2007 showing two of the eight plumes

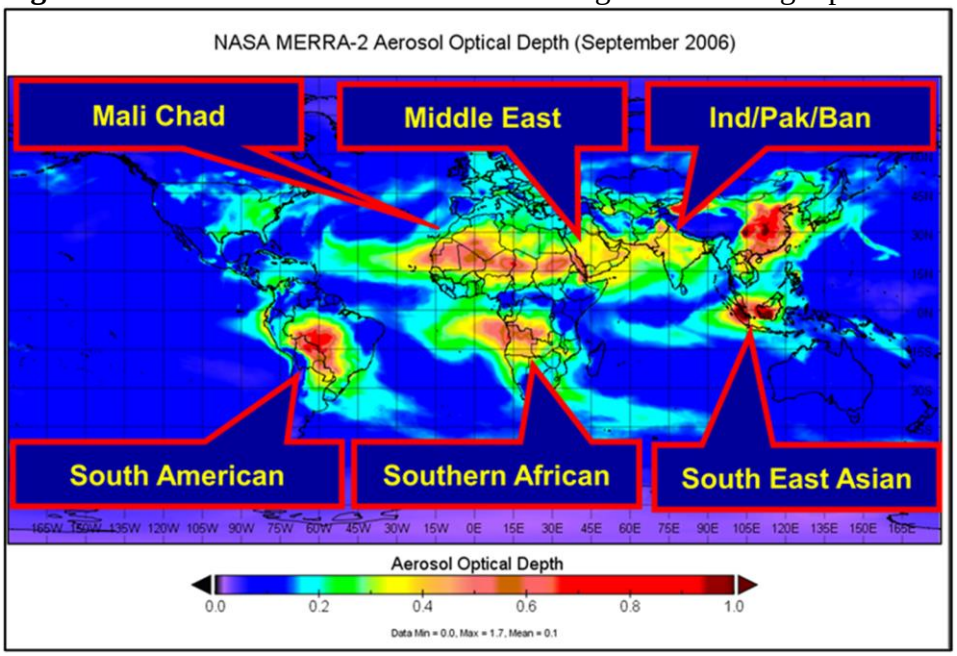

Figure B2. MERRA-2 AOD September 2006 showing six of the eight plumes

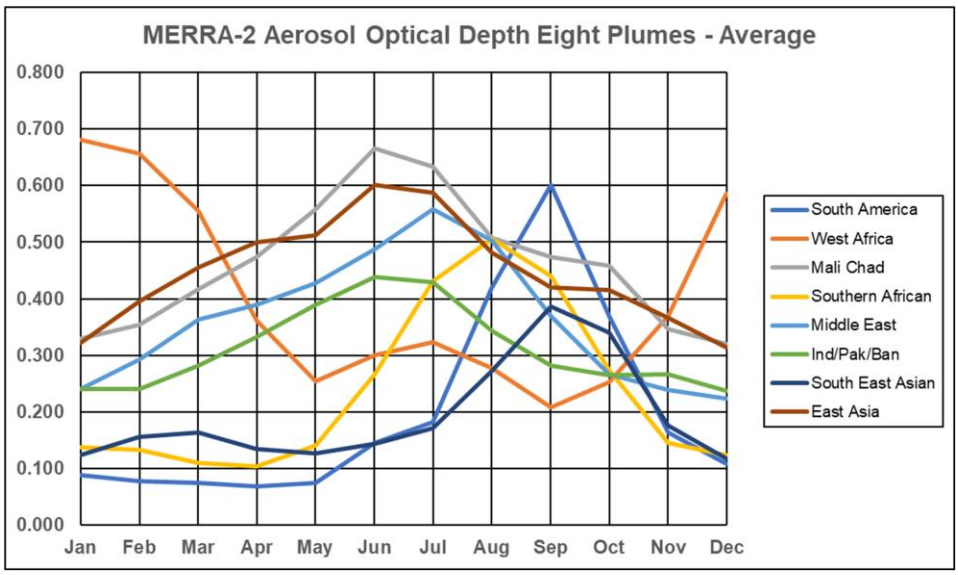

Figure B3. Average monthly MERRA-2 AOD of the eight plumes 1980 to 2020

Plume	Anthropogenic Source	Natural Source
South American	Biomass	Volcanoes
West African	Biomass, Gas Flares	Dust, Volcanoes
Mali/Chad	Peat fires under dried up lakes?	Dust
Middle East	Gas Flares	Dust, Volcanoes
Southern African	Biomass	Volcanoes, Dust
India/Pakistan/Bangladesh	Biomass, Industry	Dust
South East Asian	Biomass, Gas Flares	Volcanoes
East Asian	Industry, Biomass	Dust

Table B1. The major aerosol sources of the eight continental scale aerosol plumes

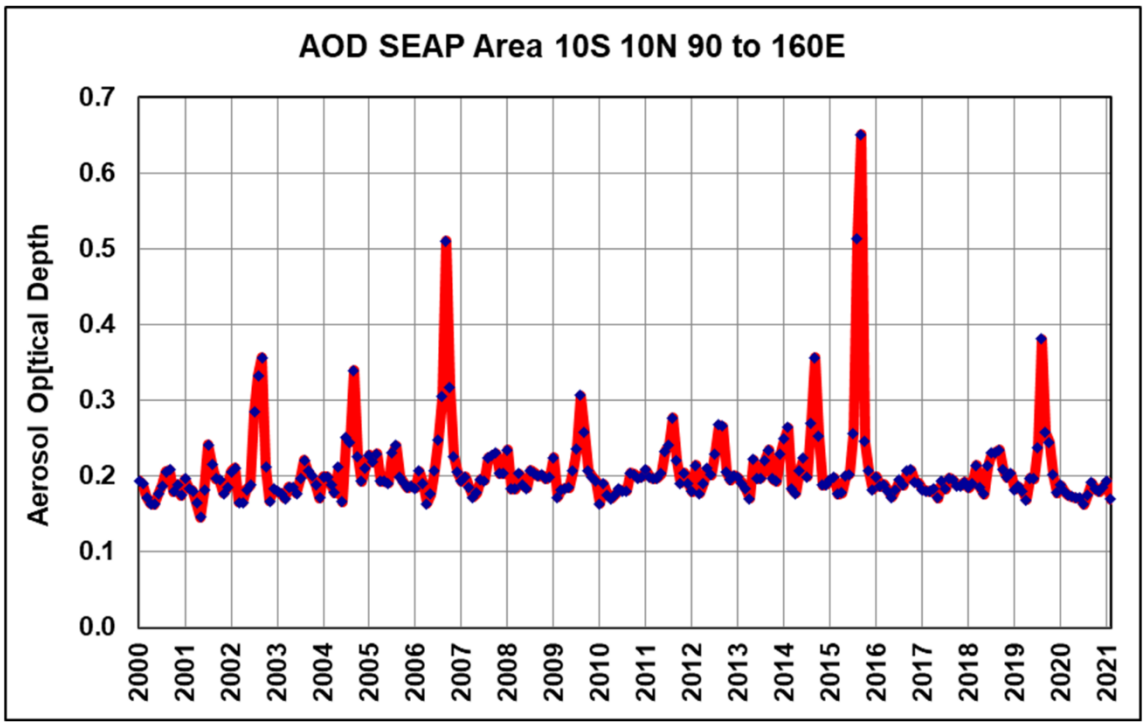

Figure B4. Monthly average MODIS Terra AOD in the CSEAP Area 5º S-5º N and 100º E-120º E.

9.1 Biomass Burning

Biomass burning in the tropics is part of the annual agricultural cycle and usually occurs at the end of the dry season before the start of the local monsoon. In the SEAP Area the monsoon commences in November and the biomass burning aerosol plume is at its most intense in SON.

The increase in biomass burning in the SEAP Area in recent decades has been driven by the increasing population of the SEAP Area. The population of Indonesia, Malaysia and Papua New Guinea has increased from 77 to 277 million between 1950 and 2010 (United Nations https://www.un.org/en/development/desa/population/publications/database/index.asp). This increasing population has forced: an increase in food production from tropical agriculture with its attendant smoke/aerosols; and increased rainforest clearing to provide living space and agricultural land. There has also been increasing levels of commercial activity including rainforest logging. In SON in 1982, 1991, 1997, 2002, 2004, 2006, 2009, 2014 and 2015 the AOD or AI increased significantly compared to the intervening years (Fig. B4 and Fig.2) due to the clearing of the rainforest for palm oil plantations.

Applegate et al. (2001) found that there was a number of direct causes of fire in the 1997-98 fires in Indonesia:

- Fire being used to assist with land clearing;
- Fire used as a weapon in land tenure or land use disputes;
- Accidental or escaped fires;
- Fire connected with resource extraction.

Neither climate change nor ENSO events are identified as a primary cause of fire in 1997-98 and the other major fire events in 1982/1983, 1987, 1991 and 1994 although this is commonly stated to be the case in the literature relating to ENSO events. ENSO is only noted as a reason for the spread of fire started by the causes noted above in certain years.

The 6th International Wildland Fire Conference held by the United Nations International Strategy for Disaster Reduction and their Food and Agriculture Organization in Korea, in 2015 released the Pyeongchang Declaration “Fire Management and Sustainable Development” (https://gfmc.online/allgemein/korea-2015.html) which stated in the Regional Statement for southeast Asia that “Most vegetation fires occurring in the member countries of the Association of Southeast Asian Nations are due to human interventions, notably by local communities and industrial corporations.”

Reports in the popular press as well as governments in the region attribute the cause of such fires to land clearing in Indonesia and on Nov 9 2006 Reuters reported “Environment ministers from five Southeast Asian countries endorsed a plan of action on Thursday to fight forest fires in Indonesia that have spread choking smoke across the region.” and “Indonesia's neighbours have grown increasingly frustrated by the fires, most of which are deliberately lit by farmers or by timber and palm oil plantation companies to clear land for cultivation.” In September 2015 the Times in London reported that “Singapore has taken legal measures against Indonesian businesses for the vast forest fires that are choking millions of people across southeast Asia.” See CIFOR at https://forestsnews.cifor.org/37016/clearing-the-smoke-the-causes-and-consequences-of-indonesias-fires?fnl=en which states that 115,000 fires were burning in Indonesia in October 2015.

The connection between AOD in the CSEAP Area and fire is demonstrated in three ways:

One: The burned areas in Indonesia from NASA at https://search.earthdata.nasa.gov/projects?p=C1457414586-SEDAC!C1457414586-SEDAC&pg[1][v]=t&pg[1][m]=download&q=burned%20area%20indonesia&tl=1563231391!4!

! (Center for International Earth Science Information Network - CIESIN - Columbia University, 2018) from 1997 to 2015 was extracted. Correlating the MERRA-2 AOD in SON, the burning season, with the areas burned in Indonesia gives 0.96 significance <0.01. The data is shown in Fig. B5

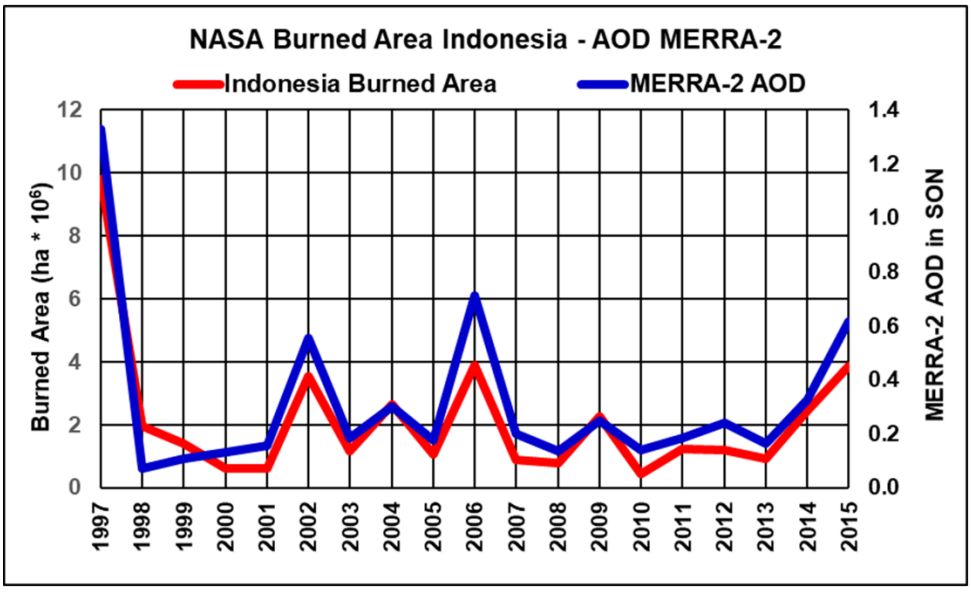

Figure B5. NASA MERRA-2 AOD in SON and area burned.

Two: The NASA MODIS FIRMS (Fire Information for Resource Management Systems) at https://firms.modaps.eosdis.nasa.gov/ from November 2000 to 2020 for Indonesia was downloaded. The daily total number of fire locations was calculated and then the average number per month was then calculated to avoid double counting fires identified on more than one day. The resulting fire count data for all months and the SON average is shown in Fig. B6 with trend lines, R^2 and trend line equation. The "all months" and SON datasets show correlations between the CSEAP AOD and fire count of 0.91 and 0.98 respectively significance < 0.01 for both. Fig. B6 clearly shows significant increases in AOD as the fire count increases - +0.5 and +0.7 per 1,000 fire count increase respectively. The CSEAP AOD is used in this analysis as the fire count is for Indonesia and the CSEAP Area covers most of Sumatra and Borneo the location of the majority of the fires.

Note: The three highest monthly AOD levels in Fig. B4 are all in SON (Oct 2006 and Sept and Oct 2015)

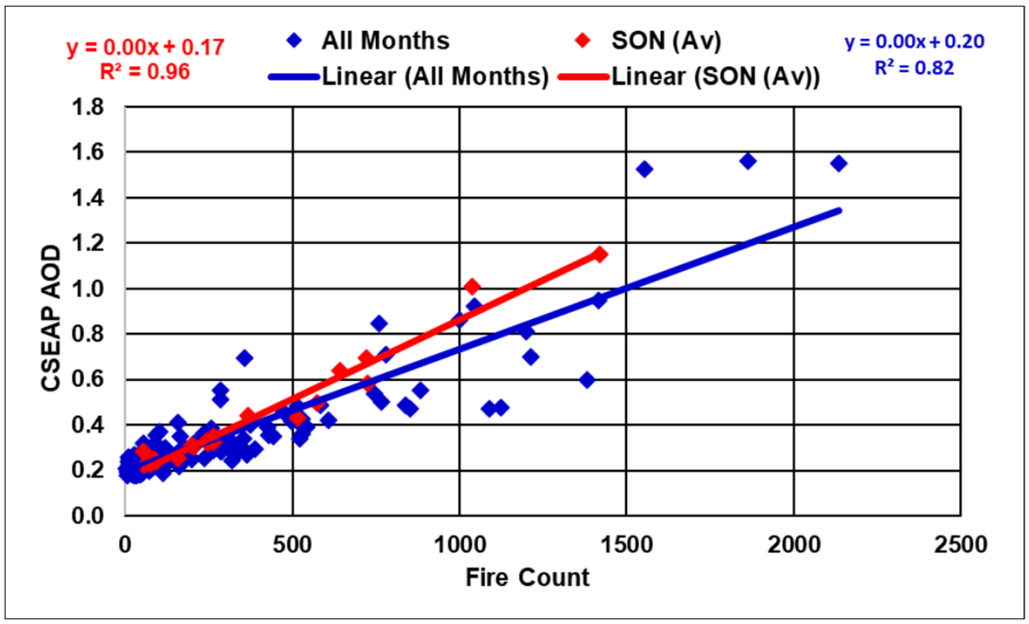

Figure B6. NASA fire information for resource management (Indonesia) and CSEAP AOD

Three: Correlating the Black Carbon (BC) Emissions from the Global Fire Emissions Database (GFED4.1) (Randerson et al., 2017) for the Equatorial Asian (EQAS) Region and of similar extent to the SEAP Area) from fires at https://daac.ornl.gov/cgi-bin/dsviewer.pl?ds_id=1293 for the period 1997 to 2020 with the SON AOD of the CSEAP Area gives 0.96. The data is shown in Fig. B7.

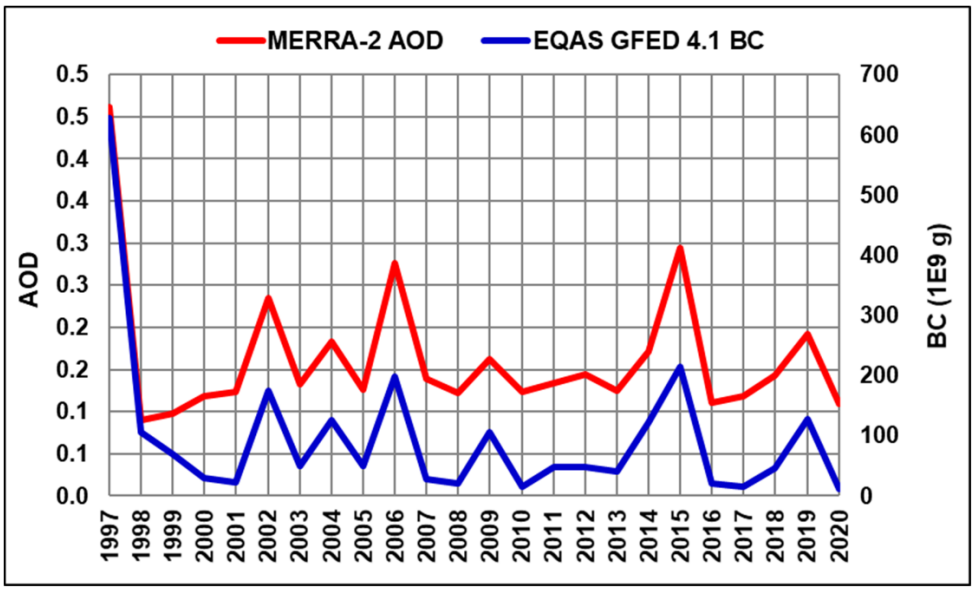

Figure B7. Equatorial Asian region black carbon emissions from the GFED database 4.1 and the CSEAP Area SON MERRA-2 AOD.

9.2 Conclusion

Together the burned area, fire and BC data show that the extreme AOD in SON in some years is created by fires in south east Asia, mainly Indonesia.

9.3 Gas flares

Gas Flares in the oil production industry increased in number over recent decades as oil production in south east Asia (Indonesia, Malaysia, Thailand and Brunei) increased from 567,000 to 1,856,000 barrels of oil per day between 1965 and 2020 (BP Statistical Review of World Energy 2021). Reid et al. (2013) discuss the composition of the SEAP.

The World Bank has established the GGFRP which estimates SE Asia flares 4.03 billion m^3 of natural gas each year and the gas flare locations are shown in Fig. 1. NOAA identifies about 387 flare locations in the SEAP Area. Images of such flares producing aerosols are easily found in Google Earth (Fig. B8) or at the GGFRP web site.

Figure B8. LNG Badak. Credits: Left Ridho Akbari, Right Fauzi (from Google Earth)

10 APPENDIX C: SCHEMATICS OF THE CREATION OF AN ENSO EVENT

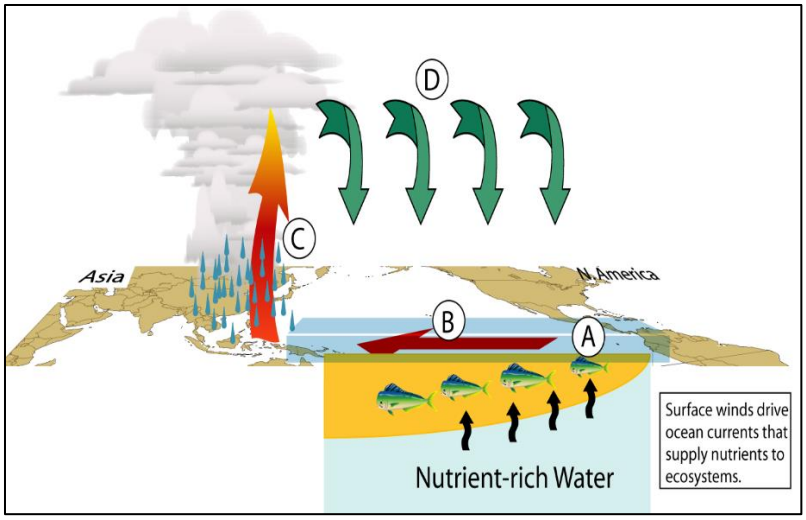

Figure C1. Schematic from NOAA showing normal Walker Circulation

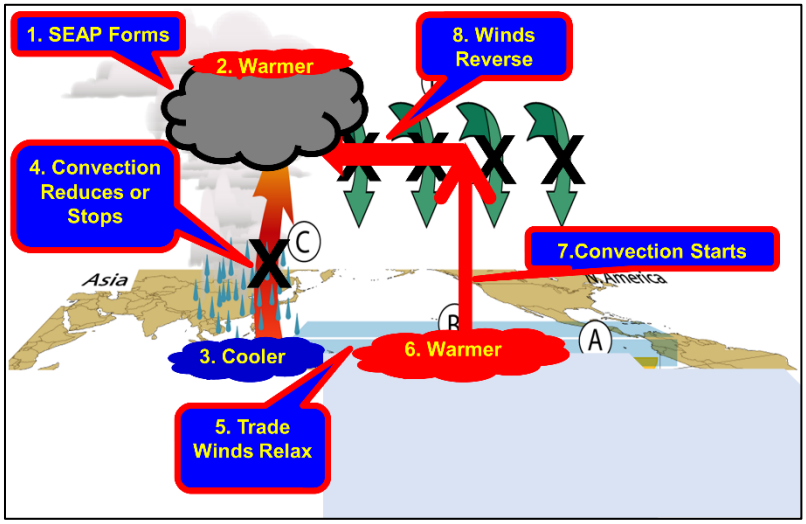

Figure C2. Schematic after NOAA showing the stages in the development of an ENSO event.

The original image in Fig. C1 and C2 was downloaded from NOAA some years ago and is no longer available. NOAA – National Oceanic and Atmospheric Administration.

11 APPENDIX D: VOLCANO DATA PROCESSING

The volcanic eruption data was downloaded from the Global Volcanism Program database at https://volcano.si.edu/list_volcano_holocene.cfm (Venzke, 2013). Then:

- Eruptions from 1870 were extracted;
- The Volcanic Explosivity Index (VEI) was extracted. Any eruptions without a listed VEI were allocated a VEI of 0;
- VEI was converted to Tephra (VEIT) in Km^3 using the table in Newhall and Self (1982) which is a pseudo logarithmic scale – level 2 is 100 times greater than level 1 whilst all other levels increase by a factor of 10;
- The eruption start year was extracted;
- The eruption start month was extracted. Eruptions with no start month were allocated sequentially to January then February and so on;
- The end year and month was extracted. For eruptions with no end date the end date was calculated using the start date and the median eruption length in (Simkin & Siebert, 2000) of 7 weeks (2 months);
- The length of each eruption in months was calculated;
- The average monthly VEIT for each eruption was calculated and allocated equally to each month of the eruption starting with the start month and ending with the end month.
- The VEIT for each month from 1870 to 2020 was summed;
- The monthly VEIT was summed to give annual VEIT data;
- In all the analyses except for the SEAus pressure and rainfall the annual VEIT data was allocated to segments and averaged and the corresponding monthly Nino or associated parameter was allocated to the same segment and averaged;
- For the SEAus pressure and rainfall only, the analysis covered the months from April to October as this is the wet season in SEAus. The monthly values were summed to give a value for each year;
- The VEIT, on a logarithmic scale, and the Nino and associated parameters were then displayed on scatter plots with the trend line, trend line equation and R^2 value.

12 APPENDIX E: – CORRELATION MATRIX FOR LME AND MERRA-2

	850	All	GHG	Land Use	Orbital	Aerosol	Solar	Volcanic	MERRA-2
850	1.00	0.02	0.02	-0.03	0.08	-0.05	0.04	-0.03	-0.22
All	0.02	1.00	0.02	-0.02	-0.05	0.09	-0.04	-0.03	0.19
GHG	0.02	0.02	1.00	0.01	0.06	-0.02	0.03	0.00	0.06
Land Use	-0.03	-0.02	0.01	1.00	-0.01	0.00	0.01	0.03	0.06
Orbital	0.08	-0.05	0.06	-0.01	1.00	0.16	0.00	0.02	-0.20
Aerosol	-0.05	0.09	-0.02	0.00	0.16	1.00	-0.07	-0.05	-0.16
Solar	0.04	-0.04	0.03	0.01	0.00	-0.07	1.00	-0.07	0.40
Volcanic	-0.03	-0.03	0.00	0.03	0.02	-0.05	-0.07	1.00	-0.27
MERRA-2	-0.22	0.19	0.06	0.06	-0.20	-0.16	0.40	-0.27	1.00
Average	-0.02	0.02	0.02	0.01	0.01	-0.01	0.04	-0.05	-0.02

Table D1: Correlation matrix for LME and MERRA-2 SEAP AODVIS/AOD. The average excludes the self-correlations which return 1.00.

Code/Data Availability

No code is required to recreate the data sets used which are all publicly available and are shown in section 3.3.

I used Matlab (Matlab, 2019) to extract and process data and create maps.

Competing Interests

The author declares that he has no conflict of interest.

The author and his wife Julie funded this research project

Author Contribution

There are no co-authors.

13 Acknowledgments

I acknowledge:

The Global Volcanism Program at the Smithsonian Institution for the volcano eruption data at https://volcano.si.edu/

NASA: Analyses and visualizations used in this paper were produced with the Giovanni online data system, developed and maintained by the NASA GES DISC;

The mission scientists and Principal Investigators who provided the data used in this paper including the CALIPSO data;

Dr Robert Schmunk for the Panoply data viewer;

Earth Observatory for the image of Sangeang Volcano;

The Indonesian burned areas data;

BC Emissions for the Equatorial Asian Region;

Indonesian fire numbers

And Oak Ridge National Laboratory for the Global Fire Emissions Database (GFED4.1s)

The Hadley Centre for the HadISST_1 dataset;

Google Earth™ and the copyright holders noted for the image of the Earth and gas flares;

The Global Forest Watch for fire data;

The Climate and Global Dynamics Division of ESSL at NCAR for the NCEP/NCAR reanalysis SEAP SST, Omega and Niño 1+2 and 3.4 SST, trade wind and SEAus pressure data;

NOAA: for the ENSO and IOD data at https://psl.noaa.gov/gcos_wgsp/Timeseries/; the trade wind and gas flare data; and for the data and images from https://psl.noaa.gov/data/gridded/reanalysis/

University Corporation for Atmospheric Research for the LME and HadlSST_1 ENSO return frequency graphs at http://webext.cgd.ucar.edu/Multi-Case/CVDP_repository/cesm1.lm/nino34.powspec.png

The CESM1(CAM5) Last Millennium Ensemble Community Project and supercomputing resources provided by NSF/CISL/Yellowstone;

The Volcano Global Risk Identification and Analysis Project for the Toba data

The United Nations Department of Economic and Social Affairs Population Division for the world population statistics;

The Australian Bureau of Meteorology for: the ENSO and Walker Circulation images; SOI data; SOI formula at http://www.bom.gov.au; and Melbourne rainfall and pressure data;

The IPCC for their assessment reports;

The U.S. Geological Survey for the earthquake information;

BP https://www.bp.com/en/global/corporate/energy-economics/statistical-review-of-world-energy.html for the oil production statistics;

The Global Gas Flaring Reduction Partnership for the gas flaring data

14 References

Abram, N. J., Wright, N. M., Ellis, B., Dixon, B. C., Wurtzel, J. B., England, M. H., et al. (2020). Coupling of Indo-Pacific climate variability over the last millennium. *Nature, 579*(7799), 385-392. https://doi.org/10.1038/s41586-020-2084-4

Ammann, C. M., Meehl, G. A., Washington, W. M., & Zender, C. S. (2003). A monthly and latitudinally varying volcanic forcing dataset in simulations of 20th century climate. *Geophysical Research Letters, 30*(12), n/a-n/a. http://dx.doi.org/10.1029/2003GL016875

Applegate, G., Chokkalingam, U., & Suyanto. (2001). The Underlying Causes and Impacts of Fires in South-east Asia. *Center for International Forestry Research and International Centre for Research in Agroforestry*.

Barry, R. G., & Chorley, R. J. (2010). *Atmosphere Weather and Climate* Routledge, Abingdon UK.

Bjerknes, J. (1969). ATMOSPHERIC TELECONNECTIONS FROM THE EQUATORIAL PACIFIC1. *Monthly Weather Review, 97*(3), 163-172. http://dx.doi.org/10.1175/1520-0493(1969)097<0163:ATFTEP>2.3.CO;2

Blake, S. A. P., Lewis, S. C., LeGrande, A. N., & Miller, R. L. (2018). Assessing the impact of large volcanic eruptions of the last millennium (850–1850 CE) on Australian rainfall regimes. *Clim. Past, 14*(6), 811-824. https://www.clim-past.net/14/811/2018/

Booth, B. B., Dunstone, N. J., Halloran, P. R., Andrews, T., & Bellouin, N. (2012). Aerosols implicated as a prime driver of twentieth-century North Atlantic climate variability. *Nature, 484*(7393), 228-232. http://www.ncbi.nlm.nih.gov/pubmed/22498628

Brown, J. N., & Fedorov, A. V. (2010). How Much Energy Is Transferred from the Winds to the Thermocline on ENSO Time Scales? *Journal of Climate, 23*(6), 1563-1580. Article. http://alumni.library.adelaide.edu.au/login?url=http://search.ebscohost.com/login.aspx?direct=true&db=a2h&AN=48558589&site=ehost-live

Cai, W., Santoso, A., Wang, G., Yeh, S.-W., An, S.-I., Cobb, K. M., et al. (2015). ENSO and greenhouse warming. *Nature Clim. Change, 5*(9), 849-859. Review. http://dx.doi.org/10.1038/nclimate2743

Cane, M. A. (2005). The evolution of El Niño, past and future. *Earth and Planetary Science Letters, 230*(3–4), 227-240. http://www.sciencedirect.com/science/article/pii/S0012821X04007083

Center for International Earth Science Information Network - CIESIN - Columbia University. (2018). *Global Fire Emissions Indicators, Country-Level Tabular Data: 1997-2015*. Retrieved from: https://doi.org/10.7927/H4V69GJ5

Dijkstra, H. A. (2006). The ENSO phenomenon: theory and mechanisms. *Adv. Geosci., 6*, 3-15. https://adgeo.copernicus.org/articles/6/3/2006/

Duncan, B. N., Bey, I., Chin, M., Mickley, L. J., Fairlie, T. D., Martin, R. V., & Matsueda, H. (2003). Indonesian wildfires of 1997: Impact on tropospheric chemistry. *Journal of Geophysical Research: Atmospheres, 108*(D15), 4458. http://dx.doi.org/10.1029/2002JD003195

Emile-Geay, J., Seager, R., Cane, M. A., Cook, E. R., & Haug, G. H. (2008). Volcanoes and ENSO over the Past Millennium. *Journal of Climate, 21*(13), 3134-3148. Article. http://alumni.library.adelaide.edu.au/login?url=http://search.ebscohost.com/login.aspx?direct=true&db=a2h&AN=33190216&site=ehost-live

Enfield, D. B. (1989). El Niño, past and present. *Reviews of Geophysics, 27*(1), 159-187. http://dx.doi.org/10.1029/RG027i001p00159

Fadnavis, S., Müller, R., Chakraborty, T., Sabin, T. P., Laakso, A., Rap, A., et al. (2021). The role of tropical volcanic eruptions in exacerbating Indian droughts. *Scientific Reports, 11*(1), 2714. https://doi.org/10.1038/s41598-021-81566-0

Gao, C., Robock, A., & Ammann, C. (2008). Volcanic forcing of climate over the past 1500 years: An improved ice core-based index for climate models. *Journal of Geophysical Research: Atmospheres, 113*(D23). https://agupubs.onlinelibrary.wiley.com/doi/abs/10.1029/2008JD010239

Gelaro, R., McCarty, W., Suárez, M. J., Todling, R., Molod, A., Takacs, L., et al. (2017). The Modern-Era Retrospective Analysis for Research and Applications, Version 2 (MERRA-2). *Journal of Climate, 30*(14), 5419-5454. https://journals.ametsoc.org/doi/abs/10.1175/JCLI-D-16-0758.1

Grothe, P. R., Cobb, K. M., Liguori, G., Di Lorenzo, E., Capotondi, A., Lu, Y., et al. (2020). Enhanced El Niño–Southern Oscillation Variability in Recent Decades. *Geophysical Research Letters, 47*(7), e2019GL083906. https://agupubs.onlinelibrary.wiley.com/doi/abs/10.1029/2019GL083906

Hammer, Ø., Harper, D. A. T., & Ryan, P. D. (2001). PAST: Paleontological statistics software package for education and data analysis. . *Palaeontologia Electronica 4(1): 9pp*, 9pp.

Handler, P., & Andsager, K. (1990). Volcanic aerosols, El Niñmo and the Southern Oscillation. *International Journal of Climatology, 10*(4), 413-424. http://dx.doi.org/10.1002/joc.3370100409

Hansell, R. A., Tsay, S. C., Ji, Q., Liou, K. N., & Ou, S. C. (2003). Surface aerosol radiative forcing derived from collocated ground-based radiometric observations during PRIDE, SAFARI, and ACE-Asia. *Appl Opt, 42*(27), 5533-5544. http://www.ncbi.nlm.nih.gov/pubmed/14526843

Hirono, M. (1988). On the trigger of El Niño Southern Oscillation by the forcing of early El Chichón volcanic aerosols. *Journal of Geophysical Research: Atmospheres, 93*(D5), 5365-5384. http://dx.doi.org/10.1029/JD093iD05p05365

Hourdin, F. d. r., Mauritsen, T., Gettelman, A., Golaz, J.-C., Balaji, V., Duan, Q., et al. (2017). The Art and Science of Climate Model Tuning. *Bulletin of the American Meteorological Society, 98*(3), 589-602. https://journals.ametsoc.org/view/journals/bams/98/3/bams-d-15-00135.1.xml

Huang, B., Thorne, P. W., Banzon, V. F., Boyer, T., Chepurin, G., Lawrimore, J. H., et al. (2017). Extended Reconstructed Sea Surface Temperature, Version 5 (ERSSTv5): Upgrades, Validations, and Intercomparisons. *Journal of Climate, 30*(20), 8179-8205. https://journals.ametsoc.org/doi/abs/10.1175/JCLI-D-16-0836.1

Kalnay, E., Kanamitsu, M., Kistler, R., Collins, W., Deaven, D., Gandin, L., et al. (1996). The NCEP/NCAR 40-Year Reanalysis Project. *Bulletin of the American Meteorological Society, 77*(3), 437-471. http://dx.doi.org/10.1175/1520-0477(1996)077<0437:TNYRP>2.0.CO;2

Kaufman, Y. J., Holben, B. N., Tanré, D., Slutsker, I., Smirnov, A., & Eck, T. F. (2000). Will aerosol measurements from Terra and Aqua Polar Orbiting satellites represent the daily aerosol abundance and properties? *Geophysical Research Letters, 27*(23), 3861-3864. http://dx.doi.org/10.1029/2000GL011968

Keeling, C. D., Piper, S. C., Bacastow, R. B., Wahlen, M., Whorf, T. P., Heimann, M., & Meijer, H. A. (2005). Atmospheric CO2 and 13CO2 Exchange with the Terrestrial Biosphere and Oceans from 1978 to 2000: Observations and Carbon Cycle Implications. In I. T. Baldwin, M. M. Caldwell, G. Heldmaier, R. B. Jackson, O. L. Lange, H. A. Mooney, E. D. Schulze, U. Sommer, J. R. Ehleringer, M. Denise Dearing, & T. E. Cerling (Eds.), *A History of Atmospheric CO2 and Its Effects on Plants, Animals, and Ecosystems* (pp. 83-113). New York, NY: Springer New York.

Khodri, M., Izumo, T., Vialard, J., Janicot, S., Cassou, C., Lengaigne, M., et al. (2017). Tropical explosive volcanic eruptions can trigger El Niño by cooling tropical Africa. *Nature Communications, 8*(1), 778. https://doi.org/10.1038/s41467-017-00755-6

Kleeman, R., & Moore, A. M. (1997). A Theory for the Limitation of ENSO Predictability Due to Stochastic Atmospheric Transients. *Journal of the Atmospheric Sciences, 54*(6), 753-767. https://journals.ametsoc.org/view/journals/atsc/54/6/1520-0469_1997_054_0753_atftlo_2.0.co_2.xml

Maher, N., McGregor, S., England, M. H., & Gupta, A. S. (2015). Effects of volcanism on tropical variability. *Geophysical Research Letters, 42*(14), 6024-6033. http://dx.doi.org/10.1002/2015GL064751

Mann, M. E., Cane, M. A., Zebiak, S. E., & Clement, A. (2005). Volcanic and Solar Forcing of the Tropical Pacific over the Past 1000 Years. *Journal of Climate, 18*(3), 447-456. http://dx.doi.org/10.1175/JCLI-3276.1

Matlab. (2019). Matlab 2019b (Version 2019b). Natick, Massachusetts:: The MathWorks Inc.

McPhaden, M. J., Busalacchi, A. J., Cheney, R., Donguy, J.-R., Gage, K. S., Halpern, D., et al. (1998). The Tropical Ocean-Global Atmosphere observing system: A decade of progress. *Journal of Geophysical Research: Oceans, 103*(C7), 14169-14240. http://dx.doi.org/10.1029/97JC02906

McPhaden, M. J., Zebiak, S. E., & Glantz, M. H. (2006). ENSO as an Integrating Concept in Earth Science. *Science, 314*(5806), 1740-1745. http://science.sciencemag.org/content/sci/314/5806/1740.full.pdf

Mignot, J., Hourdin, F., Deshayes, J., Boucher, O., Gastineau, G., Musat, I., et al. (2021). The Tuning Strategy of IPSL-CM6A-LR. *Journal of Advances in Modeling Earth Systems, 13*(5), e2020MS002340. https://agupubs.onlinelibrary.wiley.com/doi/abs/10.1029/2020MS002340

Morice, C. P., Kennedy, J. J., Rayner, N. A., Winn, J. P., Hogan, E., Killick, R. E., et al. (2021). An Updated Assessment of Near-Surface Temperature Change From 1850: The HadCRUT5 Data Set. *Journal of Geophysical Research: Atmospheres, 126*(3), e2019JD032361. https://agupubs.onlinelibrary.wiley.com/doi/abs/10.1029/2019JD032361

Newhall, C. G., & Self, S. (1982). The volcanic explosivity index (VEI) an estimate of explosive magnitude for historical volcanism. *Journal of Geophysical Research: Oceans, 87*(C2), 1231-1238. http://dx.doi.org/10.1029/JC087iC02p01231

Nicholls, N. (1988). Low latitude volcanic eruptions and the El Niño-Southern Oscillation. *Journal of Climatology, 8*(1), 91-95. http://dx.doi.org/10.1002/joc.3370080109

Nicholls, N. (1990). Low-latitude volcanic eruptions and the El Niñmo/Southern Oscillation: A reply. *International Journal of Climatology, 10*(4), 425-429. http://dx.doi.org/10.1002/joc.3370100410

Nozawa, T., Nagashima, T., Shiogama, H., & Crooks, S. A. (2005). Detecting natural influence on surface air temperature change in the early twentieth century. *Geophysical Research Letters, 32*(20), n/a-n/a. http://dx.doi.org/10.1029/2005GL023540

Ott, L., Duncan, B., Pawson, S., Colarco, P., Chin, M., Randles, C., et al. (2010). Influence of the 2006 Indonesian biomass burning aerosols on tropical dynamics studied with the GEOS-5 AGCM. *Journal of Geophysical Research: Atmospheres, 115*(D14), D14121. http://dx.doi.org/10.1029/2009JD013181

Otto-Bliesner, B. L., Brady, E. C., Fasullo, J., Jahn, A., Landrum, L., Stevenson, S., et al. (2016). Climate Variability and Change since 850 CE: An Ensemble Approach with the Community Earth System Model. *Bulletin of the American Meteorological Society, 97*(5), 735-754. http://journals.ametsoc.org/doi/abs/10.1175/BAMS-D-14-00233.1

Planton, Y. Y., Guilyardi, E., Wittenberg, A. T., Lee, J., Gleckler, P. J., Bayr, T., et al. (2021). Evaluating Climate Models with the CLIVAR 2020 ENSO Metrics Package. *Bulletin of the American Meteorological Society, 102*(2), E193-E217. https://journals.ametsoc.org/view/journals/bams/102/2/BAMS-D-19-0337.1.xml

Predybaylo, E., Stenchikov, G. L., Wittenberg, A. T., & Zeng, F. (2017). Impacts of a Pinatubo-size volcanic eruption on ENSO. *Journal of Geophysical Research: Atmospheres, 122*(2), 925-947. https://agupubs.onlinelibrary.wiley.com/doi/abs/10.1002/2016JD025796

Rajeev, K., Parameswaran, K., Nair, S. K., & Meenu, S. (2008). Observational evidence for the radiative impact of Indonesian smoke in modulating the sea surface temperature of the equatorial Indian Ocean. *Journal of Geophysical Research: Atmospheres, 113*(D17). https://agupubs.onlinelibrary.wiley.com/doi/abs/10.1029/2007JD009611

Ramanathan, V. (2006). ATMOSPHERIC BROWN CLOUDS: HEALTH, CLIMATE AND AGRICULTURE IMPACTS. *Scripta Varia 106*.

Randerson, J. T., Van Der Werf, G. R., Giglio, L., Collatz, G. J., & Kasibhatla, P. S. (2017). Global Fire Emissions Database, Version 4.1 (GFEDv4). In: ORNL Distributed Active Archive Center.

Rayner, N. A., Parker, D. E., Horton, E. B., Folland, C. K., Alexander, L. V., Rowell, D. P., et al. (2003). Global analyses of sea surface temperature, sea ice, and night marine air temperature since the late nineteenth century. *Journal of Geophysical Research: Atmospheres, 108*(D14). https://agupubs.onlinelibrary.wiley.com/doi/abs/10.1029/2002JD002670

Reid, J. S., Hyer, E. J., Johnson, R. S., Holben, B. N., Yokelson, R. J., Zhang, J., et al. (2013). Observing and understanding the Southeast Asian aerosol system by remote sensing: An initial review and analysis for the Seven Southeast Asian Studies (7SEAS) program. *Atmospheric Research, 122*, 403-468. https://www.sciencedirect.com/science/article/pii/S0169809512001809

Remer, L. A., Chin, M., DeCola, P., Feingold, G., Halthore, R., Kahn, R. A., et al. (2009). Executive Summary, in Atmospheric Aerosol Properties and Climate Impacts, A Report by the U.S. Climate Change Science Program and the Subcommittee on Global Change Research [Mian Chin, Ralph A. Kahn, and Stephen E. Schwartz (eds.)]. National Aeronautics and Space Administration, Washington, D.C., USA.

Robock, A., Taylor, K. E., Stenchikov, G. L., & Liu, Y. (1995). GCM evaluation of a mechanism for El Niño triggering by the El Chichón ash cloud. *Geophysical Research Letters, 22*(17), 2369-2372. http://dx.doi.org/10.1029/95GL02065

Saji, N. H., Goswami, B. N., Vinayachandran, P. N., & Yamagata, T. (1999). A dipole mode in the tropical Indian Ocean. *Nature, 401*(6751), 360-363.

Schmidt, G. A., Bader, D., Donner, L. J., Elsaesser, G. S., Golaz, J. C., Hannay, C., et al. (2017). Practice and philosophy of climate model tuning across six US modeling centers. *Geosci. Model Dev., 10*(9), 3207-3223. https://gmd.copernicus.org/articles/10/3207/2017/

Self, S., Rampino, M. R., Zhao, J., & Katz, M. G. (1997). Volcanic aerosol perturbations and strong El Niño events: No general correlation. *Geophysical Research Letters, 24*(10), 1247-1250. http://dx.doi.org/10.1029/97GL01127

Senior, C. A., Jones, C. G., Wood, R. A., Sellar, A., Belcher, S., Klein-Tank, A., et al. (2020). U.K. Community Earth System Modeling for CMIP6. *Journal of Advances in Modeling Earth Systems, 12*(9), e2019MS002004. https://agupubs.onlinelibrary.wiley.com/doi/abs/10.1029/2019MS002004

Simkin, T., & Siebert, L. (2000). Earth's volcanoes and eruptions: an overview p. 249-261. . In S. H (Ed.), *Encyclopedia of Volcanoes*, . San Diego: Academic Press.

Solomon, S., Qin, D., Manning, M., Z. Chen, Marquis, M., Averyt, K. B., et al. (2007). *IPCC, 2007: Climate Change 2007: The Physical Science Basis. Contribution of Working Group I to the Fourth Assessment Report of the Intergovernmental Panel on Climate Change*. Retrieved from Cambridge, United Kingdom:

Stein, K., Timmermann, A., Schneider, N., Jin, F.-F., & Stuecker, M. F. (2014). ENSO Seasonal Synchronization Theory. *Journal of Climate, 27*(14), 5285-5310. https://journals.ametsoc.org/view/journals/clim/27/14/jcli-d-13-00525.1.xml

Stocker, T. F., D. Qin, G.-K. Plattner, L.V. Alexander, S.K. Allen, N.L. Bindoff, et al. (2013). *Technical Summary. In: Climate Change 2013: The Physical Science Basis. Contribution of Working Group I to the Fifth Assessment Report of the Intergovernmental Panel on Climate Change*. Retrieved from Cambridge, United Kingdom and New York, NY, USA.:

Sturman, A. P., & Tapper, N. J. (1996). The Weather and Climate of Australia and New Zealand. Oxford University Press Australia 476.

Takemura, T., Nozawa, T., Emori, S., Nakajima, T. Y., & Nakajima, T. (2005). Simulation of climate response to aerosol direct and indirect effects with aerosol transport-radiation model. *Journal of Geophysical Research: Atmospheres, 110*(D2), n/a-n/a. http://dx.doi.org/10.1029/2004JD005029

Timbal, B., Arblaster, J., Braganza, K., Fernandez, E., Hendon, H., Murphy, B., et al. (2010). Understanding the anthropogenic nature of the observed rainfall decline across south-eastern Australia. *Centre for Australian Weather and Climate Research, Technical Report 026*.

Timbal, B., & Drosdowsky, W. (2013). The relationship between the decline of Southeastern Australian rainfall and the strengthening of the subtropical ridge. *International Journal of Climatology, 33*(4), 1021-1034.

Timmreck, C. (2012). Modeling the climatic effects of large explosive volcanic eruptions. *Wiley Interdisciplinary Reviews: Climate Change, 3*(6), 545-564. https://onlinelibrary.wiley.com/doi/abs/10.1002/wcc.192

1400 Tosca, M. G., Diner, D. J., Garay, M. J., & Kalashnikova, O. V. (2015). Human-caused fires limit convection in
1401 tropical Africa: First temporal observations and attribution. *Geophysical Research Letters*, *42*(15),
1402 2015GL065063. http://dx.doi.org/10.1002/2015GL065063

1403 Trenberth, K. E., Caron, J. M., Stepaniak, D. P., & Worley, S. (2002). Evolution of El Niño–Southern Oscillation
1404 and global atmospheric surface temperatures. *Journal of Geophysical Research: Atmospheres*, *107*(D8),
1405 AAC 5-1-AAC 5-17. http://dx.doi.org/10.1029/2000JD000298

1406 Trenberth, K. E., Stepaniak, D. P., & Caron, J. M. (2000). The Global Monsoon as Seen through the Divergent
1407 Atmospheric Circulation. *Journal of Climate*, *13*(22), 3969-3993.
1408 http://journals.ametsoc.org/doi/abs/10.1175/1520-
1409 0442%282000%29013%3C3969%3ATGMAST%3E2.0.CO%3B2

1410 Ummenhofer, C. C., England, M. H., McIntosh, P. C., Meyers, G. A., Pook, M. J., Risbey, J. S., et al. (2009). What
1411 causes southeast Australia's worst droughts? *Geophysical Research Letters*, *36*(4).

1412 USGS. (2021). *United States Geologic Survey Earthquake database*. Retrieved from:
1413 https://earthquake.usgs.gov/earthquakes/search/

1414 Venzke, E. (2013). *Volcanoes of the World. v. 4.9.1 (17 Sep 2020)* *http://dx.doi.org/10.5479/si.GVP.VOTW4-2013*.

1415 Wang, B., & An, S. (2002). A mechanism for decadal changes of ENSO behavior: roles of background wind
1416 changes. *Climate Dynamics*, *18*(6), 475-486. http://dx.doi.org/10.1007/s00382-001-0189-5

1417 Wang, C. (2002). Atmospheric Circulation Cells Associated with the El Nin˜o–Southern Oscillation. *Journal of*
1418 *Climate*.

1419 Wang, C. (2018). A review of ENSO theories. *National Science Review*, *5*(6), 813-825.
1420 https://doi.org/10.1093/nsr/nwy104

1421 Winker, D. M., Vaughan, M. A., Omar, A., Hu, Y., Powell, K. A., Liu, Z., et al. (2009). Overview of the CALIPSO
1422 Mission and CALIOP Data Processing Algorithms. *Journal of Atmospheric and Oceanic Technology*,
1423 *26*(11), 2310-2323. https://journals.ametsoc.org/doi/abs/10.1175/2009JTECHA1281.1

1424 Zebiak, S. E., & Cane, M. A. (1987). A Model El Ni&ntilde–Southern Oscillation. *Monthly Weather Review*,
1425 *115*(10), 2262-2278. http://journals.ametsoc.org/doi/abs/10.1175/1520-
1426 0493%281987%29115%3C2262%3AAMENO%3E2.0.CO%3B2

1427 Zhang, D., Blender, R., & Fraedrich, K. (2013). Volcanoes and ENSO in millennium simulations: global impacts
1428 and regional reconstructions in East Asia. *Theoretical & Applied Climatology*, *111*(3/4), 437-454. Article.
1429 http://alumni.library.adelaide.edu.au/login?url=http://search.ebscohost.com/login.aspx?direct=true&db=a2h
1430 &AN=85133626&site=ehost-live

1431